

# Electronic effects on the radiation damage in high-entropy alloys

Okan K. Orhan,<sup>1</sup> Mohamed Hendy,<sup>1</sup> and Mauricio Ponga<sup>1,\*</sup>

<sup>1</sup>*Department of Mechanical Engineering, University of British Columbia,  
2054 - 6250 Applied Science Lane, Vancouver, BC, V6T 1Z4, Canada*

High-entropy alloys (HEAs) are exceptional candidates for radiation-resistant materials due to their complex local chemical environment and slow defect migration. Despite commonly overlooked, electronic effects on defects evolution in radiation environments also play a crucial role by dissipating excess energy through electron-phonon coupling and electronic heat conduction during cascade events. We present a systematic study on electronic properties in random-solid solutions (RSS) in four and five principal elements HEAs and their effect on defect formation, clustering, and recombination. Electronic properties, including electron-phonon coupling factor ( $G_{e-ph}$ ), the electronic specific heat ( $C_e$ ), and the electronic thermal conductivity ( $\kappa_e$ ), are computed within first-principles calculations. Using the two-temperature molecular dynamics simulations, we show that the electron-phonon coupling factor and electronic specific heat play a critical role in Frenkel pairs formation. Specifically, the electron-phonon coupling factor quickly dissipates the kinetic energy during primary knock-on atom events via plasmon excitations and is subsequently dissipated via the free-electrons conduction. We show that these effects are more critical than the elastic distortion effects produced by the atomic mismatch. Of tremendous interest, we show that including lighter elements helps to increase  $G_{e-ph}$  suggesting the possibility to improve radiation resistance in HEA through optimal composition.

## I. INTRODUCTION

High-entropy alloys (HEA) are single-phased multi-principal-elements (MPE) alloys, often produced by *nearly* equimolar mixing of four, or more elements [1–3]. HEAs have been shown to exhibit exceptional thermal stability [4], hardness and strength [5–10], wear resistance [11, 12], and oxidation resistance [11, 13]. In particular, the equimolar chromium-cobalt-iron-nickel HEA (CrFeCoNi) has attracted considerable interest as it can serve as a base template to exploring non-equimolar compositions, or adding other elements such as manganese (Mn), copper (Cu), aluminum (Al), titanium (Ti), niobium (Nb), molybdenum (Mo) and many more to achieve exceptional materials properties [1, 14–19, 21].

In high-radiation environments, highly energetic particle beams excite primary knock-on atoms (PKAs) out when they travel through solids, which in turn create self-interstitial atoms (SIA) and vacancies, called Frenkel pairs (FPs). Formation and clustering of FPs locally distort lattices, resulting in dislocation loops and void growth. As these FPs recombine and migrate through the lattice, they generate significant microstructural changes over time, critically affecting the mechanical properties of materials subjected to radiation environments. Clustering of defected atoms commonly reduces the structural integrity of materials by causing swelling, creep, and irradiation-induced stress corrosion cracking [22].

In the case of HEA, the complex local chemical environment and atomic-size mismatch create well-known elastic lattice distortions and core effects such as sluggish diffusion kinetics [3]. These effects help to reduce defect

formation, slow down defect diffusion and accumulation, and promote vacancy-interstitial recombination, leading to lower radiation damage compared to pure metals and traditional alloys [23, 24]. For instance, CrMnFeCoNi preserves its majority face-centered cubic phase even over 40 DPA irradiation throughout the temperature range of  $\sim 298 - 773$  K [25]. Thus, HEAs are promising candidates for structural materials exposed to high-radiation environments [18, 26] such as in nuclear reactors [18, 27] and other environments such as space applications [26].

Due to the many challenges that appear during the testing of materials under radiation environments, experimental studies are difficult to perform and time-consuming. At the same time, since the formation, migration, clustering, as well as recombination of defects occur within a few femtoseconds (fs) to nanoseconds (ns) of the primary cascade event, it is pretty challenging to *in-situ* unravel mechanisms behind the defect evolution. Thus, the community heavily relies on numerical simulations to understand and predict radiation damage under radiation, especially for novel materials. In that sense, atomistic simulations based on either molecular dynamics (MD) or *ab-initio* molecular dynamics provide a framework to study materials under radiation environments systematically [18, 28]. Being an atomistic technique, MD fully resolves the time and atomic environment and naturally describes the interactions between PKA and lattice, generating defects as the PKA losses its energy. These insights can then be incorporated in Monte-Carlo codes to predict damage in macroscopic specimens such as those used in engineering applications [29]. However, a drawback of classical MD is that it neglects electronic effects in materials.

In metallic materials such as HEA, the excess energy due to high-radiation exposure is deposited into phonons and electrons, resulting in defect formation and

---

\* Corresponding author: [mponga@mech.ubc.ca](mailto:mponga@mech.ubc.ca)

microstructural changes. Remarkably, the primary heat carriers in metallic materials are free electrons, which result in thermal conductivities that are much higher than the lattice contribution [30]. However, in MPE alloys, these contributions have to be carefully analyzed since they might change depending on the composition and defect population [31, 32]. Therefore, incorporating electronic effects in radiation damage is paramount for metallic materials to accurately understand and predict the damage.

Due to the potential applications of MPE alloys as radiation-resistant materials, several studies have recently investigated their performance using a combination of experiments and numerical simulations, providing a fundamental understanding of the damage mechanisms during radiation in MPE alloys [28, 33–36]. Remarkably, while the numerical simulations carried out in these studies include phonon effects in MPE alloys, electronic effects have been almost completely ignored in these works, making these results applicable -but also essentially limited- to small PKA energies. In particular, electronic effects become more predominant at moderate to high PKA energies since they trigger extremely high *electronic* temperatures, as locally observed on irradiated surfaces [37]. However, MD lacks quantum-mechanical effects required to capture electronic and electron-phonon (e – ph) coupling effects. Even though MD is a classical technique, is it possible to partially incorporate electronic effects within semi-empirical approaches such as the *so-called* two-temperature model [38–48]. However, these models require several temperature-dependent material parameters that are challenging to compute and, in many cases, remain unavailable. This lack of parameters is more accentuated in novel materials where properties are unavailable to the scientific community.

First-principles simulations provide valuable insights into the electronic properties of materials, especially in novel compositions. Unfortunately, such simulations are heavily constrained by system size and spatial complexity [49, 50]. In particular, it is challenging to accurately represent statistical representation of configurational disorderliness as in HEA cases. On the other hand, classical molecular dynamics (MD) is highly suitable for simulating the evolution of defects, in particular, to obtain statistical representation in the cases of MPE alloys such as HEAs [24, 34]. Thus, tackling the lattice dynamics within MD and electronic parts within first-principles methods provides a tractable and appealing approach.

This work presents a first-principles investigation of electronic properties in MPE alloys at several molar compositions. The temperature-dependent electron-phonon (e – ph) coupling factor ( $G_{e-ph}$ ), electronic specific heat ( $C_e$ ) and electronic thermal conductivity ( $\kappa_e$ ) are calculated within fully first-principles approaches. Additionally, the influence of the electronic effects in an equimolar CoCrFeNi HEA is investigated under radiation environments within MD simulations incorporating the electronic effects using the *local* two-temperature molecular

dynamics ( $\ell$ 2T-MD) method [46, 51]. For the first time, our work provides accurate first-principles electronic data for MPE alloys and shows the importance of these effects in radiation damage. Remarkably, we have found that neglecting these effects could lead to large overestimations of the FP population (up to  $\sim 46\%$ ) even at low PKA energies of 50 keV. An expedient model is developed to predict vacancy formation for the compositional space of Cr-Fe-Co-Ni. Temperature-dependent first-principles electronic, and phonon properties database, and MD defect-evolution database are made available in the repository at Ref. 52.

## II. THEORETICAL AND COMPUTATIONAL METHODOLOGY

### A. Calculating first-principles electronic, and phonon properties

Let us now describe the relevant parameters of interest needed to quantify the electronic effects in multi-PE alloys. The temperature-dependent e – ph coupling factor  $G_{e-ph}$  is given by [53, 54]

$$G_{e-ph} = -\frac{\pi \hbar k_B \lambda \langle \omega^2 \rangle}{g(E_F)} \int_{-\infty}^{\infty} d\epsilon \frac{\partial f(\epsilon, \mu, T_I^e)}{\partial \epsilon} g^2(\epsilon), \quad (1)$$

where  $k_B$  is the Boltzmann constant,  $g(E)$ ,  $E_F$ , and  $\mu$  are the electronic density of states (EDOS), the Fermi energy, and the chemical potential, respectively;  $f(\epsilon, \mu, T_e)$  is the Fermi-Dirac distribution function. The e – ph mass enhancement parameter,  $\lambda \langle \omega^2 \rangle$ , is given by

$$\lambda \langle \omega^2 \rangle = 2 \int_0^{\infty} d\omega \omega \alpha^2 F(\omega), \quad (2)$$

with  $\alpha^2 F(\omega)$  is the Eliashberg spectral function. The temperature-dependent electronic specific heat,  $C_e$ , is given by [54]

$$C_e = \int_{-\infty}^{\infty} d\epsilon (\epsilon - E_F) \frac{\partial f(\epsilon, \mu, T^e)}{\partial T^e} g(\epsilon). \quad (3)$$

The final component to describe the electronic properties of materials related to heat conduction, is the temperature-dependent thermal conductivity,  $\kappa_e$ , given by [37],

$$\kappa_e = v_F^2 \tau_p C_e, \quad (4)$$

where  $v_F$ , and  $\tau_p$  are the Fermi velocity, and the plasmon lifetime, respectively, which are also implicitly dependent on the electronic temperature.

The three central quantities in Eqs. (1), (3), and (4) require accurate estimation of  $g(E)$ ,  $E_F$ ,  $\lambda$  and  $\alpha^2 F(\omega)$ ,  $v_F$  and  $\tau_p$ . Kohn-Sham density-functional theory (KS-DFT) [55–59] is almost-ubiquitous first-principles ap-

proach to calculate electronic structures of solids. Its perturbative extension, called the density-functional perturbation theory (DFPT) [60, 61], also provides an expedient approach for obtaining zero-temperature phonon properties. Despite rapid advancements in underlying algorithms, and computational resources, the KS-DFT-based implementations are severely limited in terms of system size and spatial complexity, in particular for metallic systems [49, 50]. It is particularly challenging in the cases of HEAs, since it requires a large number of supercell simulations to achieve an accurate statistical representation configurational disorderliness. Virtual-crystal approximation (VCA) is an expedient approach to study multi-principles elements solids at the disordered mean-field limit [62]. Within VCA, the atomic pseudo-potentials [63] of constituent elements are linearly mixed to a single pseudopotential, representing a virtual atom [64].

As DFT is an *absolute-zero-temperature* theory, their  $T^e$ -dependence cannot be fully captured, yet it can be partially introduced through a smearing parameter around the Fermi level, representing  $T_e$ , in the case of metallic systems. With that in mind,  $g(E)$  is expected to have a negligible  $T^e$ -dependence as it only affects occupancies of the electronic states at around the Fermi level as the practical DFT assign occupancies after optimizing the KS states. It is more suitable to include the possible effects of  $T^e$  through  $E_F$  as it does not require a large number of electronic band-structure simulations. The  $T^e$ -dependent  $E_F$  can be easily obtained using the zero-temperature electronic structure with little additional computational cost. We refer the reader to Refs. 65 and 66 for details on how to obtain  $\lambda$  and  $\alpha^2 F(\omega)$ , using DFPT. The  $T^e$ -dependence can be partially introduced by setting the smearing parameter used for the double-delta integral during the e-ph coupling simulations.

Consistently, the averaged Fermi-velocity square,  $\langle v_F^2 \rangle$ , can be approximately given by [67]

$$\langle v_F^2 \rangle = \frac{\left( \sum_m \int_{S_{F_m}} d\mathbf{k} \left| \frac{\partial E_{m,\mathbf{k}}}{\partial \mathbf{k}} \right|^2 \right)}{\left( \sum_n \int_{S_{F_n}} d\mathbf{k}' \right)}, \quad (5)$$

assuming that the electronic bands have parabolic dispersions normal the Fermi surface.  $S_{F_m}$ , and  $E_{m,\mathbf{k}}$  are the partial Fermi surface, and the KS energy of the  $m$ -th metallic band, respectively. In practice,  $\langle v_F^2 \rangle$  is calculated on a slab with a thickness of  $\Delta E_{\text{Fermi}}$  using the in-house post-processing tool [68], available in Ref. 69. It requires a well-converged electronic band structure on an extremely dense Brillouin-zone sampling. The  $T^e$ -dependence can be consistently included by setting  $d_{\text{Fermi}} = k_B T^e$  [70]. We point out that Eq. (5) does not include the e-ph coupling effects, which can be introduced as the electron mass renormalization such as  $v_F \rightarrow v_F/(1 + \lambda)$  [71].

Ignoring any impurity, the plasmon lifetime of a metal-

lic solid can be expressed as the sum of the electron-electron (e-e) and the electron-phonon (e-ph) scatterings terms within Matthiessen's rule such as

$$\frac{1}{\tau_p} = \frac{1}{\tau_{e-e}} + \frac{1}{\tau_{e-ph}}. \quad (6)$$

The e-e term (in the Hz unit) can be estimated using the Fermi liquid theory at the absolute-zero temperature by [72-74]

$$\frac{1}{\tau_{e-e}} = \frac{m e^4 (E - E_F)^2}{64 \pi^3 \hbar^3 \epsilon_0 E_s^{3/2} E_F^{1/2}} \left( \frac{2 \sqrt{E_s E_F}}{4 E_F + E_s} + \arctan \sqrt{\frac{4 E_F}{E_s}} \right), \quad (7)$$

where  $m$ ,  $e$ ,  $\hbar$ , and  $\epsilon_0$  are the electronic mass, the unit charge, the reduced Plank's constant and the vacuum permittivity, respectively. The kinetic energy due to the Thomas-Fermi screening length  $q_s = e \sqrt{g(E_F)/\epsilon_0}$  given by  $E_s = \hbar^2 q_s^2 / (2m)$ . By setting  $(E - E_F) = k_B T^e$ , the  $T^e$ -dependence can be consistently introduced alongside the  $T^e$ -dependent  $E_F$ . The second term in Eq. (11) is approximately given by [65, 75]

$$\frac{1}{\tau_{e-ph}} = \frac{2\pi k_B \lambda T_e}{3}. \quad (8)$$

### 1. Computational details of first-principles simulations

First-principles simulations were performed using the Quantum ESPRESSO (QE) software [76, 77] with the external thermodynamics `thermo_pw` package [78]. Fermi velocities were calculated using an in-house code available in Ref. [69]. The SG15 optimized norm-conserving Vanderbilt (ONCV) scalar-relativistic pseudo-potentials [79, 80] (version 1.2) using the Perdew-Burke-Ernzerhof (PBE) exchange-correlation functional [81-83] were used for the four base elements (Cr, Fe, Co and Ni), as well as the additional elements (Al, Mn and Cu). Atomic pseudo-potential were used to obtain the virtual atoms representing MPEs alloys within VCA. In the case of the base-centered cubic Fe, the ONCV fully-relativistic pseudo-potential during the structural optimization, and electronic structure simulations, whereas the spin polarization was ignored during the phonon simulations due to the current limitations in the available software.

The initial crystallographic information for the thermodynamically most-stable phases of the base elements was extracted from Ref. [84]. Cr and Fe have body-centered cubic (BCC) structures, while Co and Ni have hexagonal closed-packed (HCP) and face-centered cubic (FCC) structures. The FCC Ni structure was used as a template for the initial crystal structures for the HEAs. Variable-cell relaxation was performed using a common high kinetic energy cutoff of 150 Ry on a  $12 \times 12 \times 12$  Monkhorst-Pack-equivalent Brillouin zone

sampling (MP-grid) [85], and the convergence for the total energies, the total forces, and the self-consistency were set to  $10^{-7}$  Ry,  $10^{-6}$  Ry·a<sub>0</sub><sup>-3</sup> and  $10^{-10}$ , respectively.

To practically mimic the extreme electronic temperatures of  $\sim 30000$  K on irradiated surfaces, the temperature grid was divided into two parts such as a low temperature grid of 100–1000 K with a step size of 100 K, and a high temperature grid of 3000–30000 K with a step size of 3000 K. The electronic temperatures were consistently introduced a smearing parameters around the Fermi levels in all simulations. The first set of simulations were performed to obtain anharmonic thermodynamic properties were calculated for the low- $T^e$  using the quasi-harmonic approximation [86] within the `thermo_pw` package on a shifted  $12 \times 12 \times 12$  MP-grid for electronic structure simulations, and a  $4 \times 4 \times 4$  MP-grid for phonon simulations. The e–ph mass enhancement parameters were calculated by following the procedure in Refs. 65 and 66 with a dense  $36 \times 36 \times 36$  MP-grid for interpolation, and a converged  $12 \times 12 \times 12$  MP-grid for electronic structure simulations,  $4 \times 4 \times 4$  MP-grid for phonon simulations. Finally, the Fermi velocities were calculated using the in-house code starting from the band structures, calculated on a  $36 \times 36 \times 36$  MP-grid. Temperature-dependent electronic, and phonon properties upto  $3 \times 10^4$  K have been made publicly available in the repository at Ref. 52.

## B. $\ell 2$ T-MD methodology

The  $\ell 2$ T-MD method, developed by Ullah and Ponga [46], provides computationally feasible and seamless approach to simulate the electronic effects in MD simulations within the two-temperature model. Considering a system with  $N_a$  atoms, each atom is provided with an electronic temperature variable. Let  $(T_i^e)$  denote the electronic temperature associated with the  $i$ -th atom in the system which can fluctuate locally depending on the local environments during a cascade even [87]. At the same time, let us introduce a maximum electronic temperature  $T_{\max}^e$  representing an *arbitrary* upper bound to the electronic temperature of the system. On the basis of this maximum temperature, we can map the temperature field using the transformation  $\theta_i = \frac{T_i^e}{T_{\max}^e}$  which maps  $\theta_i \in [0, 1]$  interval.

According to Ullah and Ponga [46], the  $\ell 2$ T-MD model electronic temperature evolution using the following master equation.

$$\begin{aligned} \frac{\partial T_i^e}{\partial t} = & \underbrace{\frac{G_{e-ph}}{C_e} T_{\max}^e (\theta_i^{\text{lat}} - \theta_i^e)}_{e-ph} \\ & + T_{\max}^e \underbrace{\sum_{j \neq i}^{N_a} K_{ij} \left[ \theta_j^e (1 - \theta_i^e) e^{\theta_i^e - \theta_j^e} - \theta_i^e (1 - \theta_j^e) e^{\theta_j^e - \theta_i^e} \right]}_{e-e} \end{aligned} \quad (9)$$

In Eq. (9) the time-evolution of  $T_i^e$  for each atom is influenced by the energy exchange energy between electrons surrounding the  $i$ -th atom (and denoted by (e–e)), and a coupling between electron and phonons (e–ph).  $K_{ij}$  is a material property that quantifies the rate of electronic energy exchange between electrons near two adjacent atomic sites. Interestingly,  $K_{ij}$  can be linked to well-defined properties obtained either from *ab-initio* simulations or experimental data and is going to be described below.

The term  $G_{e-ph}$  measures the e–ph scattering between electrons close to the Fermi level and phonons and determines how effectively the energy exchange between e–ph occurs. On the other hand, the term  $C_e$  determines how much excess energy electrons can absorb. By definition, both of these terms are always positive for metals. A higher  $G_{e-ph}$  leads to more rapid energy exchange between e–ph, while a higher  $C_e$  allows to store more excess energy in the free electrons. When a sudden amount of energy is introduced in the system, there is a rapid rise in the lattice temperature ( $T_i^{\text{lat}}$ ), which electrons around the Fermi level can partially absorb until the electronic and lattice temperatures reach equilibrium.

We notice that  $\theta_i^{\text{lat}} = T_i^{\text{lat}}/T_{\max}^e$  in Eq. (9) denotes a mapped local lattice temperature that is classically defined by

$$T_i^{\text{lat}} = \frac{2}{3k_B N_c} \sum_{\substack{j=1, \\ j \neq i}}^{N_c} \frac{1}{2} m_j v_j^2, \quad (10)$$

$N_c$  is the number of atoms in a small cluster surrounding the  $i$ -th atom. The small cluster is defined within a cut-off radius,  $r_c$ , which is equal to the interatomic potential's cut-off used in MD [46].  $m_j$ , and  $v_j$  are the atomic mass and the velocity vector of the  $j$ -th atom.

The pair-wise exchange-rate thermal coefficient  $K_{ij}$  for the electronic temperature can be determined by a long-wave analysis to well defined thermodynamics properties [46, 51, 88] and is given by

$$K_{ij} = \frac{2d\kappa_e}{C_e Z b^2} = \frac{2dv_F^2 \tau_P}{Zb^2}, \quad (11)$$

where  $d = 3$  is the system dimension,  $Z$  is the coordination number of the lattice without distortion, and  $b$  is the Burgers vector.

### 1. Computational details of classical molecular dynamics simulations

MD and  $\ell 2$ T-MD simulations were performed using the Large-scale Atomic/Molecular Massively Parallel Simulator (LAMMPS) software [12], into which the  $\ell 2$ T-MD have been implemented by Ullah and Ponga [46]. The  $\ell 2$ T-MD routine was modified to allow  $G_{e-ph}$ ,  $C_e$ , and  $\kappa_e$  to be updated with  $T_i^e$ . A binary search algorithm

on a hook-up table was used to find the correct parameters range corresponding to  $T_i^e$ , while linear interpolation was used to interpolate the values corresponding to the exact  $T_i^e$ . The embedded atom model (EAM) potential by Farkas and Caro [90] was used as the interatomic potential as it can model HEA of Co, Cr, Fe and Ni and was used previously in literature for modeling radiation damage for HEA [28, 91]. The electronic stopping was incorporated in the model through electron stopping fix in LAMMPS [92, 93]. The stopping-power values were calculated using the Stopping and Range of Ions in Matter (SRIM) software [94] with a minimum cut-off energy of 10 eV. The short-range interactions were modified using a ZBL potential [95] to prevent atoms from getting too close during the displacement cascades. The ZBL potential was smoothly linked to the EAM pair potential for distances between 0.05 nm and 0.18 nm. This procedure does not affect the equilibrium properties.

An initial cubic simulation cell with a dimension of  $L = 34$  nm was used to fill using a generic crystal with a lattice parameter of  $a = 0.363$  nm with a total number of atoms of 3,538,944. This cell size ensured that the radiation-induced damage was contained within the simulation cells' boundaries. Periodic boundary conditions were employed in all three directions for all simulation cells. The initial simulation cells of CoCrFeNi were obtained by randomly placing Co, Cr, Fe and Ni on the atomic sites. Then the simulation cells were subjected to energy minimization at  $T = 0$  K using the Polak-Ribière conjugate gradient algorithm [13]. Subsequently, an initial temperature of  $T = 300$  K was given to the atoms, and the system was relaxed for 30 ps using the Nosé–Hoover thermostat to relax the hydrostatic pressure to zero. The same energy minimization and relaxation procedures were used for the Ni simulation cells.

Cascade events were initiated by randomly choosing a primary knock-on-atom (PKA) located at the center of the simulation cells. The PKA was given a random velocity vector corresponding to recoil energy of 50 keV in an NVE ensemble. For the  $\ell$ 2T-MD simulation, the average lattice and the average electronic temperatures ( $T_{\text{lat}}$ , and  $T_e$ , respectively) were initially set at  $T = 300$  K before energizing the PKA. A variable time step was used with a maximum time step of  $\leq 0.01$  fs for the cascade simulations to limit the maximum distance for every time-step moved by the PKA atom to 0.005 Å. At each MD step, between 10 to 15  $T_e$  integration time-steps of Eq. (9) were performed. The total time of the cascade simulations was about 32 ps, which was sufficient for the FPs to reach steady states. Each cascade simulation was repeated eight times with different random PKA directions and HEA structures to ensure sufficient statistical representation.

The common-neighbor analysis (CNA) [97] was used to identify formations of defect clusters. The Ovito software was used for visualization of the defect structures [98], and the DXA algorithm was used for dislocation loops analysis [99]. Finally, the Wigner-Seitz defect analysis

was performed to determine the vacancies and the self-interstitial atoms (SIA) using the Ovito software.

The related database of defect evolutions in Ni, and CrFeCoNi within the conventional MD, and the  $\ell$ 2T-MD has been made publicly available in the repository at Ref. 52.

### III. RESULTS AND DISCUSSION

We start with our base HEA (CrFeCoNi) and its PEs. In Fig. 1, the mixing Gibbs free energy ( $G_{\text{mix}}$ ) and the individual contributions to it are shown up to 1000 K. The configurational-entropy contribution is the predominant term, leading to thermal stability at a low temperature. At the same time, the mixing electronic and the mixing vibrational Helmholtz free energies ( $F_{\text{el}}^{\text{mix}}$ , and  $F_{\text{vib}}^{\text{mix}}$ , respectively) are negligible (see the Supplementary Materials (SM) [100] for the details to calculate the free energies, and the configurational entropy). CrFeCoNi is also elastically stable according to the Born-Huang-stability criteria [11, 101] (see the SM [100] for further details), and dynamically stable as it has neither negative nor soft phonon modes [103].

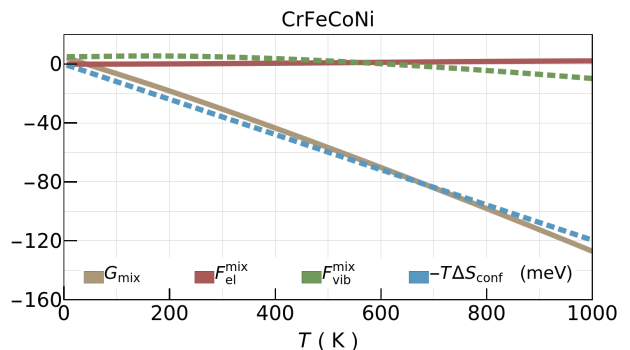


FIG. 1. Temperature dependent mixing Gibbs free energy ( $G_{\text{mix}}$ ) for CrFeCoNi in RSS. Mixing electronic, and vibrational Helmholtz free energies ( $F_{\text{el}}^{\text{mix}}$  and  $F_{\text{vib}}^{\text{mix}}$ , respectively), and the configurational-entropy contribution ( $-T\Delta S_{\text{conf}}$ ) also shown in the plot. See SM for calculations details.

In Fig. 2,  $G_{\text{e-ph}}$ ,  $C_e$ , and  $\kappa_e$  are depicted for the four pure elements, and their equimolar FCC RSS.  $G_{\text{e-ph}}$  exhibits quite similar trends for CrFeCoNi and the pure elements, exponentially vanishing with the increasing temperature. The integral term in Eq. (1) predominantly sets this trend when the individual terms are further analyzed as shown in Figs. S1 and S2. However, the non-integral terms for each system roughly average to the same order and determine magnitudes of  $G_{\text{e-ph}}$ . It becomes in order of 1 at around 500 K, indicating that electrons become too fast for e-ph scattering. On the other hand,  $C_e$  almost-linearly increases with the increasing  $T^e$ . This results to a rapid  $G_{\text{e-ph}}/C_e \rightarrow 0$  for  $T^e$  above 500 K. This indicates that there will be very little energy transfer from electrons to lattice when  $T_i^e \gg T_j^{\text{lat}}$ . On the

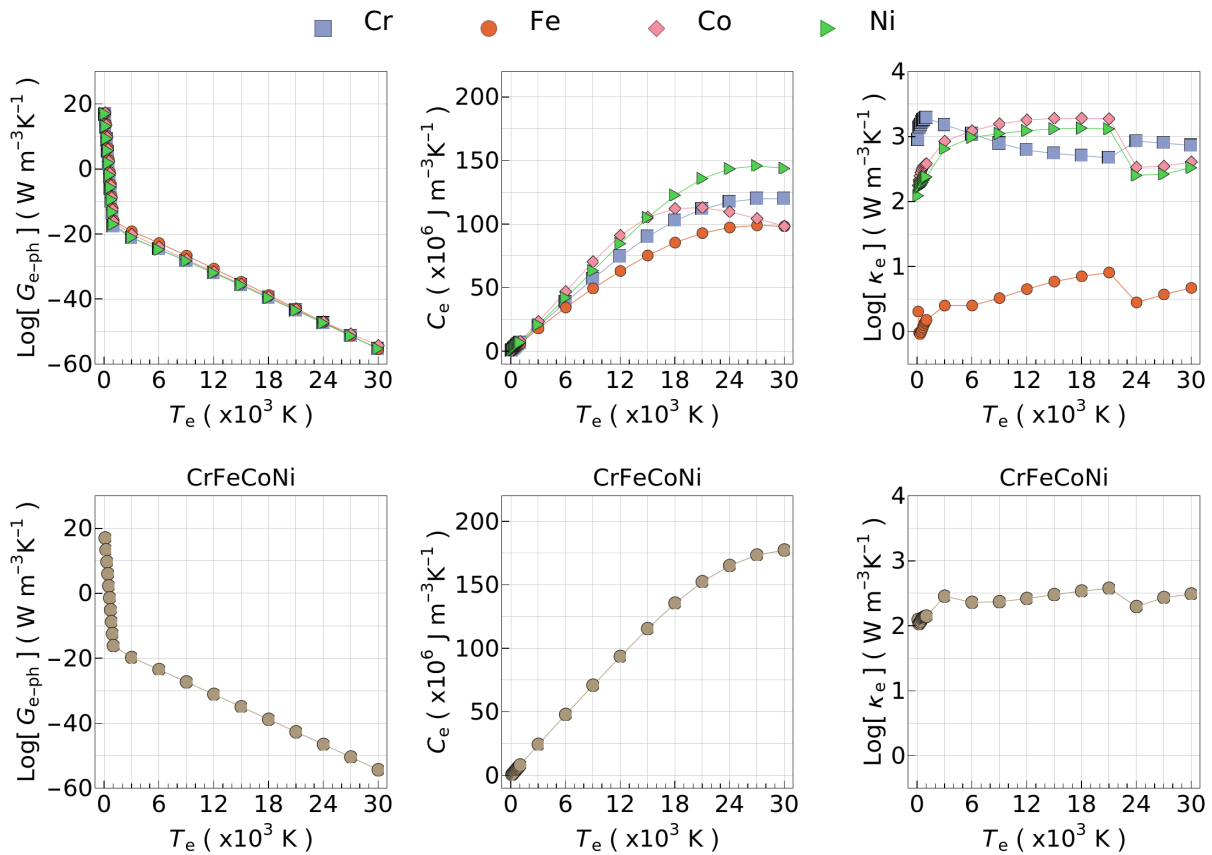


FIG. 2. Temperature dependence of the  $e - \text{ph}$  coupling factor ( $G_{e-\text{ph}}$ ), the electronic specific heat ( $C_e$ ), and the electronic thermal conductivity ( $\kappa_e$ ) of the base PEs, and the FCC CrFeCoNi.

other hand, despite also decreasing  $\kappa_e/C_e$  ratio, there will still be energy dissipation, mediated solely by electrons. This scenario is desirable to keep FPs formation by dissipating excess energy among electrons while avoiding further energizing the lattice.

Comparing  $C_e$  of CrFeCoNi with the pure elements, we observed that CrFeCoNi has a higher  $C_e$ , hinting that electrons have a better capacity to absorb energy compared to the pure metals. This effect could be important in radiation environments as the plasmons take on more thermal energy, which is removed from the lattice and thus could result in less FP formation. At lower temperatures, Cr exhibits higher  $\kappa_e$  compared to other PEs and CrFeCoNi, while CrFeCoNi, Co, and Ni performs better at higher electronic temperatures (i.e.,  $T^e \gtrsim 6000$  K). The trends in  $\kappa_e$  are predominantly determined by  $v_F$ , portrayed in Figs. S1 and S2, as well as  $\lambda$  as it renormalize  $v_F$  by including  $e - \text{ph}$  coupling effects. This effect leads to remarkable poor performance for Fe as it has the slowest  $v_F$  with the largest  $\lambda$ . Despite its not-so-superior  $\kappa_e$  when compared to those of the PEs, CrFeCoNi has a much higher  $C_e$ . It leads to a much smaller  $K_{ij} \propto v_F^2 \tau_p$ , indicating that while its electrons could hold more energy for the same electronic temperature, they are less effective in dissipating it compared to the

PEs. In summary, CrFeCoNi is expected to absorb excess lattice energy more effectively via  $e - \text{ph}$  coupling compared to the PEs, while less effective to dissipate it via  $e - e$  coupling except for Fe.

#### A. Compositional space of non-equimolar Cr-Fe-Co-Ni random solid solutions

Higher  $G_{e-\text{ph}}$  and  $C_e$  are the key factors for a superior radiation-damage resistance in HEA. Thus, a potential strategy to improve radiation damage properties is to tune molar fractions of PEs to further improve these properties. We investigate the compositional space of the Cr-Fe-Co-Ni RSS. For a systematic yet feasible investigation, we vary each PE at a time on a molar-fraction grid of  $x = [0, 0.05, 0.10, 0.15]$  while keeping the remaining three elements equimolar among themselves. The  $x = 0$  cases are the equimolar 3-PEs cases; however, the non-CrFeCoNi cases are called the non-equimolar cases for simplicity. By varying each PE one by one, the individual effect of each PE can be partially assessed, although reducing a single PE automatically increases the molar fraction of the remaining three.

The first step is to assess the relative stability of the

non-equimolar RSS. In Fig. 3, the Gibbs free energy differences ( $\Delta G$ ) of the RSS compared to the CoCrFeNi are illustrated up to 1000 K. Reducing Cr or Fe leads to thermally less stable compositions by increasing  $G$  while reducing Ni has an opposite effect. Reducing the molar-fraction of Co has a less significant effect on the thermal stability, and this is consistent with previous studies carried out in five PE alloys [21]. At room temperature (300 K), a reduction up to 20% of Cr or Fe, or a reduction of Co only leads to  $\Delta G$  in the order of 1 meV, which is in the order of the accuracy of the practical DFT simulations. Reduction of Ni already leads to better thermal stability; thus, it is thermally more favorable in any case. The non-equimolar RSS are also elastically stable according to the Born-Huang-stability criteria. They are also dynamically stable except for CoCrFe ( $\text{Ni}_x(\text{CoCrFe})_{1-x}$  for  $x = 0$ ) as it has negative phonon modes at around the X high-symmetry point in the first Brillouin zone of the primitive FCC unit cell.

In Fig. 4, dimensionless ratios  $\bar{G}_{e-\text{ph}}^x$ ,  $\bar{C}_e^x$  and  $\bar{\kappa}_e^x$  for non-equimolar compositions are shown to assess their relative performance in dissipating excess energy. The dimensionless ratios are computed as the ratio of  $G_{e-\text{ph}}$ ,  $C_e$  and  $\kappa_e$  of the non-equimolar RSS to those of CoCrFeNi. Reducing Cr concentration (first column in Fig. 4) quickly worsen  $G_{e-\text{ph}}$  and  $C_e$  starting at around the room temperature. It indicates that the lower Cr concentration can lead to less effective energy exchange between  $e-\text{ph}$ , shown to play a crucial role in promoting defect recombination and reducing defect clustering. Reducing Fe or Co concentrations (central columns in Fig. 4) have subtle effects on  $G_{e-\text{ph}}$ ,  $C_e$  and  $\kappa_e$ . On the other hand, a 25 – 50% reduction of Cr significantly improves purely electronic heat dissipation, hinted by much higher  $\kappa_e$ . However, the comparative analysis carried out later on in Section III C for Ni and CrFeCoNi indicates that the  $e-e$  term in Eq. (9) has a lesser effect on the defect evolution. At the lower temperatures ( $T < 1000$  K) (the inset figures in Fig. 4), lower Ni concentrations improve  $G_{e-\text{ph}}$  with a less significant loss in  $C_e$ . Unlike Cr, lower Ni concentrations drastically worsen  $\kappa_e$  ( $\sim 50\%$ ) at lower temperatures. The composition-dependent relative changes in  $G_{e-\text{ph}}$  are determined mainly by ratios of the electron-phonon mass enhancement parameters ( $\lambda$ ), while the ratios of the Fermi velocities primarily determine the general trends in  $\kappa_e$  ( $v_F$ ), shown in Figs. S3 - S6.

## B. Equimolar additions of Al, Mn, or Cu

Another strategy to tailor the electronic and phonon parameters is to add other elements rather than exploring non-equimolar compositions. In Fig. 5, the relative thermal stabilities of equimolar AlCrFeCoNi, CrMnFeCoNi (also known as Cantor alloy), and CrFeCoNiCu are shown with respect to CrFeCoNi. While introducing Al or Mn leads to better thermal stability, CrFeCoNiCu becomes less thermally stable. However, it is still thermally

stable in its own merit as indicated its mixing Gibbs free energy, shown in Fig. S10 using the thermal data for the elemental Cu from Ref. 70 While all three RSS are elastically stable according to the Born-Huang-stability criteria, only CrMnFeCoNi and CrFeCoNiCu are dynamically stable as AlCrFeCoNi has negative phonon modes at around L high-symmetry point in the first Brillouin zone of the primitive FCC unit cell.

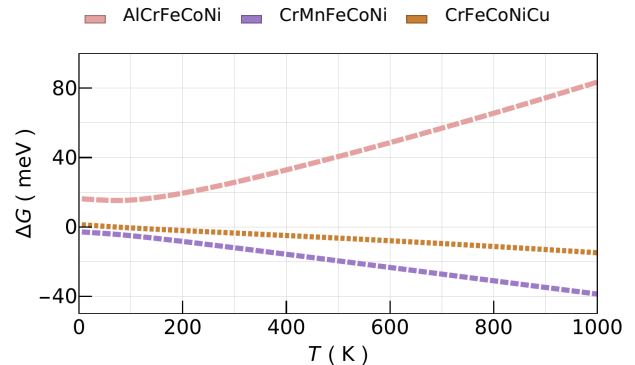


FIG. 5. Temperature dependent Gibbs free energy differences ( $\Delta G$ ) for equimolar AlCrFeCoNi, CrMnFeCoNi, and CrFeCoNiCu compared to the CrFeCoNi.

In Fig. 6, the relative performance of the electronic ( $\bar{G}_{e-\text{ph}}^{\text{Al/Mn/Cu}}$ ,  $\bar{C}_e^{\text{Al/Mn/Cu}}$  and  $\bar{\kappa}_e^{\text{Al/Mn/Cu}}$ ) properties compared to CrFeCoNi are shown. The very first observation is that the addition of Al drastically increases  $G_{e-\text{ph}}$  [104], as well as substantially increases  $C_e$  and  $\kappa_e$  by more or less  $\sim 2$  times compared to those of CrFeCoNi. On the other hand, the addition of Mn has almost-no effect on  $G_{e-\text{ph}}$ ,  $C_e$ , or  $\kappa_e$ . Finally, the addition of Cu worsens  $G_{e-\text{ph}}$  and improves  $\kappa_e \sim 1.5$  times while almost no effect on  $C_e$ .

The drastic increase in  $G_{e-\text{ph}}$  of AlCrFeCoNi is mostly due to the integral term in Eq. (1), as well as higher  $\lambda \langle \omega^2 \rangle$  and lower  $g(E_F)$ , as displayed in Figs. S8 and S7. The higher  $\lambda$  values can be mainly attributed to lower averaged mass as phonon modes are normalized with the average mass of the unit cell. On the other hand, introducing Mn, which is *most-alike* to CrFeCoNi in terms of its averaged atomic mass and VEC, has the most negligible effects on the EDOS and phonon DOS (PDOS); thus,  $G_{e-\text{ph}}$  is almost identical except at the very low temperatures. In the case of CrFeCoNiCu, the lower  $\lambda$  alongside negligible increment in other significant terms in Eq. (1), shown in Fig. S11, leads to a lower  $G_{e-\text{ph}}$ .

In the case of  $C_e$ , the EDOS is the principal figure of merit, as imposed by Eq. (3) (in particular, due to  $\mu \approx E_F$ ) When comparing the EDOS of the four systems in the top-right panel of Fig. S7, the EDOS of CrFeCoNi, CrMnFeCoNi, and CrFeCoNiCu are pretty similar. On the other hand, AlCrFeCoNi has lower yet more spread-out EDOS, leading to higher  $C_e$ . With that in mind, the higher  $\kappa_e$  of AlCrFeCoNi is due to its higher  $C_e$ , as well as its faster free electrons despite shorter-living, shown in

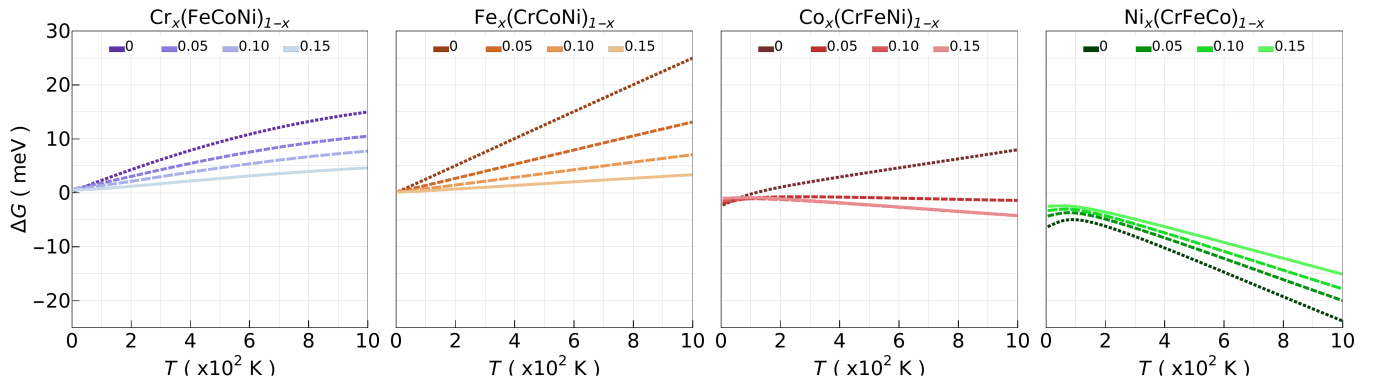


FIG. 3. Temperature dependent Gibbs free energy differences ( $\Delta G$ ) for non-equimolar compositions compared to the CrFeCoNi random solid solution.

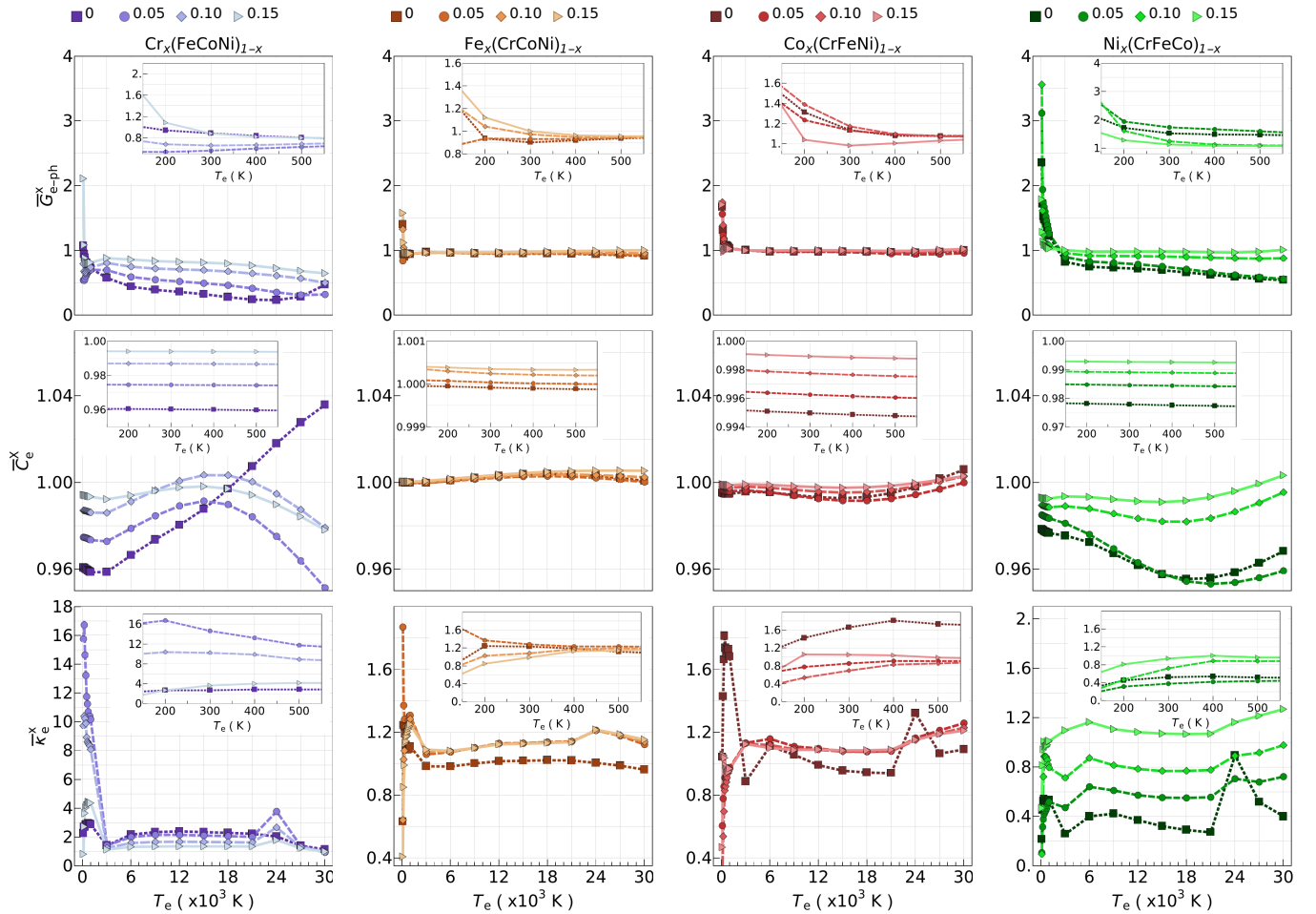


FIG. 4. Temperature dependence of the electronic property ratios for non-equimolar compositions compared to CrFeCoNi. The  $e$  –  $ph$  coupling factor ratio ( $\overline{G}_{e-ph}^x$ ), the fractional electronic specific heat ( $\overline{C}_e^x$ ), and the fractional electronic thermal conductivity ( $\overline{\kappa}_e^x$ ) fractions for non-equimolar random-solid solutions compared to CrFeCoNi.

Fig. S8. Without any contribution from  $C_e$ , the almost-identical  $\kappa_e$  of CrMnFeCoNi is due to counter-balancing of changes in  $v_F$  and  $\tau_p$ . On the other hand, CrFeCoNiCu has faster as well as longer living plasmons, leading to slightly higher  $\kappa_e$ . As  $\tau_p$  is inversely proportional to  $\lambda$

via Eq. (8), which is the predominant term in Eq. (11), a higher  $\lambda$  leads to a lower  $\tau_p$ . Similarly,  $v_F$  is renormalized by  $(1 + \lambda)$ , a higher  $\lambda$  lower it. However, a steeper band dispersion can compensate for this reduction, as in the case of AlCrFeCoNi.



When introducing additive elements, the relative changes in  $G_{e-ph}$  and  $\kappa_e$  are determined by both electronic and phonon properties, while  $C_e$  is purely electronic. In the case of  $\kappa_e$ , it is also dependent on fine details of electronic band dispersion and Fermi surface.

### C. Benchmark: Defect evolution in Ni and CrFeCoNi

Despite its relatively well-scalability, accurate MD simulations are still computationally challenging, particularly to achieve a reasonable statistical representation of HEAs. Thus, the elemental Ni and CrFeCoNi are chosen as the benchmark cases to simulate the defect evolution.

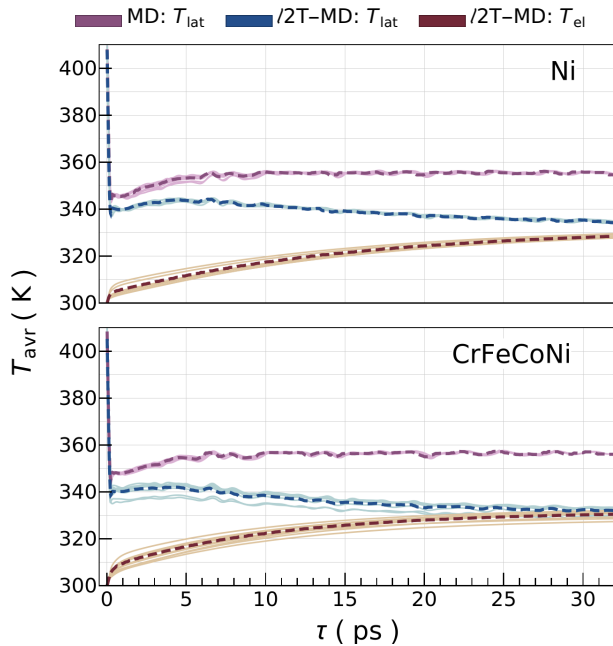


FIG. 7. Time evolution of the average lattice ( $T_{lat}$ ) and electronic ( $T_e$ ) temperatures for Ni and CrFeCoNi within the conventional MD and  $l2T$ -MD for a 50 keV PKA. The mean values of the repeated eight simulations are shown with dashed lines.

We start by analyzing the time evolution of the average temperatures depicted in Fig. 7. For both materials, the initial average  $T_{lat}$  spike to  $\sim 408$  K from the initial 300 K due to the additional kinetic energy of PKA. We also notice that for the  $l2T$ -MD simulations, the average electronic temperature also shown in Fig. 7 remains at 300 K at  $t = 0$  ps. For classic MD and  $l2T$ -MD simulations, the lattice temperature showed a quick dip at around  $\sim 0.25$  ps in  $T_{lat}$  (listed in Table S1) as the PKA transfer energy to the surrounding atoms and rapidly generated defects. After that, the lattice temperature quickly stabilizes near a steady-state value that is very similar for MD simulations (355 K and 356 K for Ni and CoCrFeNi, respectively).

On the other hand, examining the  $l2T$ -MD simulations, we observed a much different behavior. For those simulations incorporating the electronic effects, the lattice temperature continuously reduced its value as time went by, whereas the electronic temperature monotonically increased. These two temperatures eventually reached equilibrium (at 334 K and 332 K for Ni and CoCrFeNi, respectively) at around  $t = 32$  ps. We also observed that the standard deviation of these values was around  $\pm 2$  K, illustrating a very robust statistical response of the multiple replicas used in the study. The analysis of the average temperature of the system with time suggests subtle differences between Ni and CoCrFeNi, and thus, it is beneficial to investigate the evolution of the maximum temperatures during the simulations.

Fig. 8 compares the maximum local lattice and electronic temperatures during the cascade simulations within  $l2T$ -MD simulations. At first glance, we observed that the peak of lattice temperature was the same for both materials, whereas the peak for the electronic temperature was different (see insets in Fig. 8). The time to reach the maximum electronic temperature ( $\sim 0.05$  ps) is comparable with plasmon lifetime  $\tau_p$  and could hint at ballistic heat conduction in the electrons near the PKA for both materials. While ballistic heat conduction is neglected here, we point out that the  $l2T$ -MD implementation allows for second sound simulations, and a computational implementation is provided in Refs. [51, 88]. We also observed for CoCrFeNi several oscillations in the maximum electronic temperature, hinting at local plasmon excitations during the PKA trajectory. As a result, and considering that the width of the peak was much longer for the CoCrFeNi compared to Ni, the lattice temperature dropped faster for CoCrFeNi than Ni. These facts hint at a better energy exchange between  $e-ph$  for CoCrFeNi compared with the pure metal. Indeed, the energy exchange between electrons and phonon is more significant in the case of CrFeCoNi as indicated more prolonged survival of  $T^e$  before reaching steady temperatures (at around 30 ps) compared to those of Ni, reaching steady temperatures at around 15 ps.

To better understand this energy exchange, Fig. 9 shows a graphical comparison of the local electronic properties between CrFeCoNi and Ni for the first  $t = 2$  ps using the maximum electronic temperature. Remarkably, the ratio between  $G_{e-ph}$  for CrFeCoNi and Ni is much greater than one below  $t = 0.5$  ps, and eventually converged to two; suggesting a much faster exchange of thermal energy from the lattice to the electrons. Moreover,  $C_e$  is about 20% greater for CrFeCoNi compared to Ni although some variations are observed below  $t = 0.5$  ps. Only the thermal conductivity of the high entropy alloy is less than Ni (about 70% of Ni), but it seems to have a much less critical impact on the thermodynamics behavior of the two subsystems.

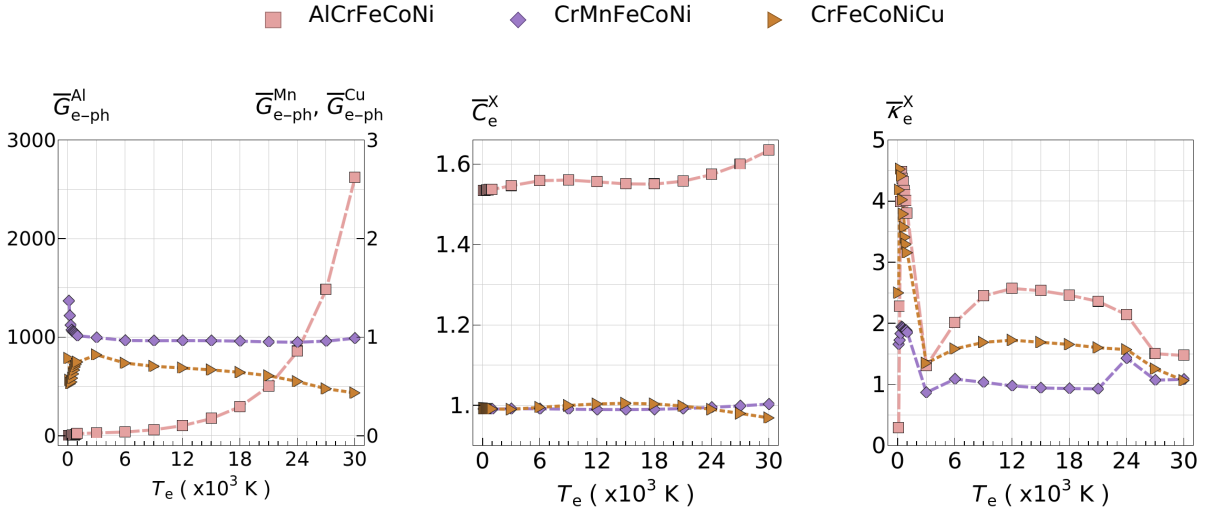


FIG. 6. Temperature dependence of the electron-phonon coupling factor ( $G_{e-ph}$ ), electronic specific heat ( $C_e$ ), and electronic thermal conductivity ( $\kappa_e$ ) fractions of AlCrFeCoNi, CrMnFeCoNi, and CrFeCoNiCu compared to CrFeCoNi. Note that  $G_{e-ph}^{Al}$  scale is shown at the left of the plot.

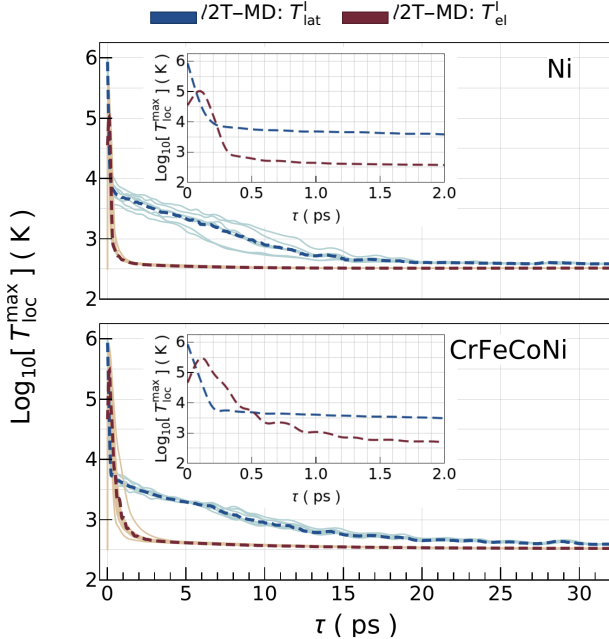


FIG. 8. Time evolution of the maximum local lattice temperatures ( $T_{lat}^I$ ), electronic temperatures ( $T_e^I$ ) of Ni and CrFeCoNi within the  $l2T$ -MD for a 50 keV PKA. The mean values of the repeated simulations are shown with dashed lines.

### 1. Electronic effects in defect formation and recombination

Having analyzed the evolution of the electronic and lattice temperatures during the simulations, we now investigate the impact on defect formation when electronic effects are included. Fig. 10 depicts the time evolution of the defected atoms and FP in the simulations. Defected atoms are defined as those atoms that do not belong to

the FCC lattice. Qualitatively, the trends are very similar for defected atoms and FPs. An initial high-peak was observed at the earlier stages of the simulations, i.e.,  $\tau_{def}^{max} = 0.31$  ps (listed in Table I). A monotonic decay of defected atoms and FP followed until the number stabilized after  $\tau^{steady} = 8 - 10$  ps. The number of defected atoms and FP was higher for all MD simulations compared to the  $l2T$ -MD simulations, and also for Ni compared to CoCrFeNi (cf.  $N_{def}^{steady}$  and  $N_{FP}^{steady}$  in Table I columns one and two, and three and four). At the initial stages of the cascade events, the steep decrease in  $T_{lat}$  leads to a rapid defected-atom generation as indicated by the sharp increase in the total number of defected atoms ( $N_{def}$ ) in Fig. 10. The reduced number of FP compared to defected atoms indicates that during the early stages of the PKA, some defects form FP while some are only partially defected due to lattice distortions or recombine quickly due to the high local thermal energy. Nevertheless, besides reducing significantly after a few ps, FPs reached steady-state for all simulations after  $\sim 10$  ps.

As shown in Table I the trends are analogous as the number of defected atoms with more FP for MD compared to  $l2T$ -MD and for Ni to CoCrFeNi. Interestingly, comparing the FP at the end of the simulations, a difference of  $\sim 17\%$  was observed for Ni, and this is comparable with previous studies for pure metals [43–46]. Difference can be attributed to the temperature dependence implemented in our work compared to previous ones, where usually  $C_e$  and  $\kappa_e$  are modeled as a linearly dependent on  $T_e$ . However, as shown in Fig. 2, this is only true for moderate temperature ranges and both quantities saturate at high temperatures. Comparing the FP for CoCrFeNi, the incorporation of electronic effects resulted in  $96 \pm 5$  FPs, whereas classical MD showed  $140 \pm 24$ , or a difference of 45% between the two approaches. The sig-

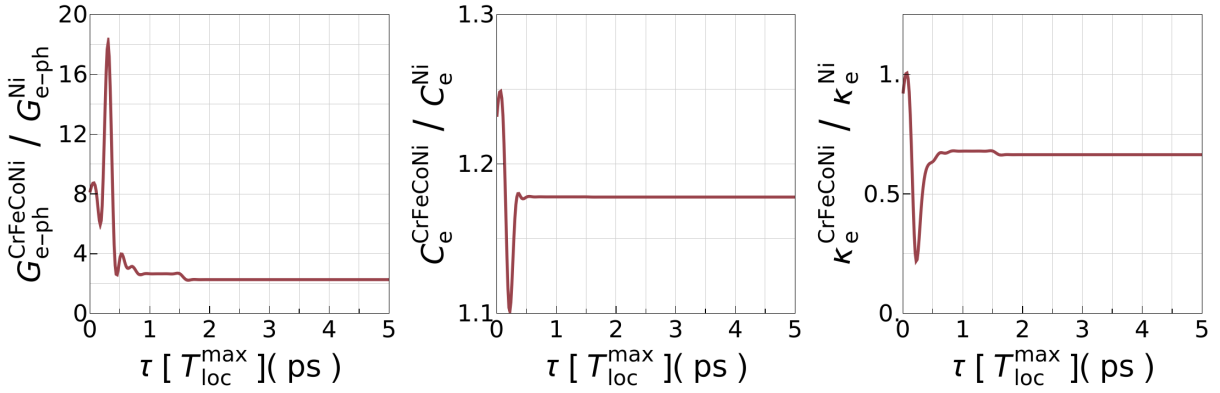


FIG. 9. Time evolution of the  $e - \text{ph}$  coupling factor ( $G_{e-\text{ph}}$ ), the electronic specific heat ( $C_e$ ), and the electronic thermal conductivity ( $\kappa_e$ ) ratios between Ni and CrFeCoNi.

nificantly higher  $G_{e-\text{ph}}$  of CrFeCoNi compared to that of Ni, shown in Fig. 9, significantly promote higher defect recombination, leading to lower FPs at steady-state.

It is evident from Fig. 10 that the electronic effects shorten the time scale to reach the steady states FPs. Thus, we conclude that the electronic effects play a more critical role in determining the final number of FPs after the PKA, and these effects are more critical than those made by the elastic distortions present in high-entropy alloys. To better explain this finding, we computed the SIA ( $s_f^1$ ) and vacancy formation ( $v_f^1$ ) energies in the HEA and compared to Ni and these results are shown in Fig. S12 and Fig. S13 and listed in Table S2. For instance, the vacancy formation energy in CoCrFeNi has a Gaussian distribution owing to the elastic distortions. However, when analyzed on average, we observed that the formation energy  $v_f^1 \approx 1.64$  eV which is very close to one in Ni,  $v_f^1 = 1.56$  eV. These small differences suggest that the energetic cost of generating a vacancy is not strongly affected by the elastic distortions and thus, cannot drastically reduce FPs formation during the PKA event.

These findings are in line with previous results obtained by Deluigi *et al.* [28] where the effect of the elastic distortions was investigated and compared to an equivalent mean-field discrete sample. Noteworthy, Deluigi *et al.* [28] concluded that the elastic distortion plays a minor role in the generation of FP during low energy PKA events. Even though these authors did not include electronic thermal effects, we observe similar trends here. These results illustrate the importance of the electronic effects in MD and justify their inclusion besides increasing the simulations' computational cost.

## 2. Electronic effects in defect clustering

Another important factor in comparing the classical MD and  $\ell$ 2T-MD simulations is the size of the defected cluster resulting after the cascade simulations. To this end, we graphically represented the cluster size (as de-

noted by the defected atoms in different defect clusters in the simulations) for twenty clusters as shown in Fig. 11 and also visualized in Fig. S14. Again, results for MD and  $\ell$ 2T-MD for Ni and CoCrFeNi are compared.

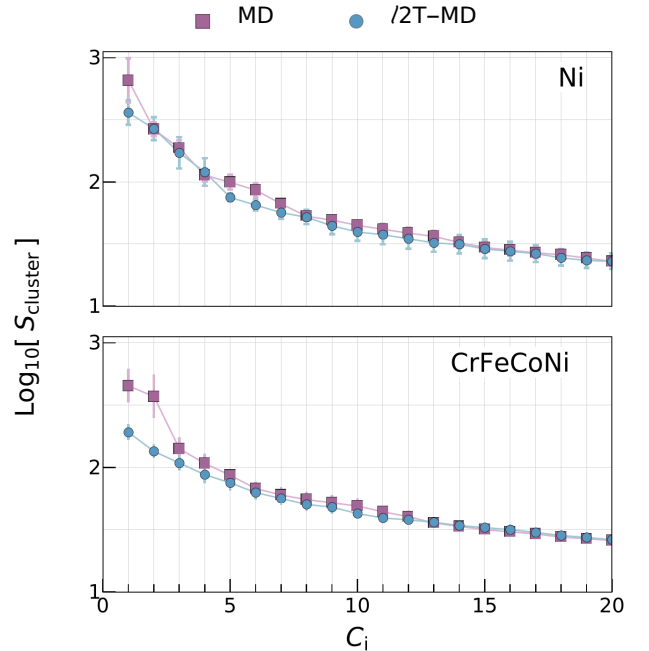


FIG. 11. Comparison of the defect cluster size ( $S_{\text{cluster}}$ ) for each cluster in descending order of size ( $C_i$ ) in Ni, and CrFeCoNi within the conventional MD and the  $\ell$ 2T-MD simulations for a 50 keV PKA.

Ni generates larger defect clusters without the electronic effects, as much as  $\sim 1.5$  times larger ones than those of CrFeCoNi. When the electronic effects are included, this ratio rises to  $\sim 2$ . Smaller  $S_{\text{cluster}}$  in CoCrFeNi compared to Ni can be attributed to better energy exchange between  $e - \text{ph}$  ( $G_{e-\text{ph}}$ ) and heat capacity ( $C_{e-\text{ph}}$ ). Remarkably, the lower values of thermal conductivity ( $\kappa_e^{\text{CrFeCoNi}}$ , displayed in Fig. 9) of the high en-

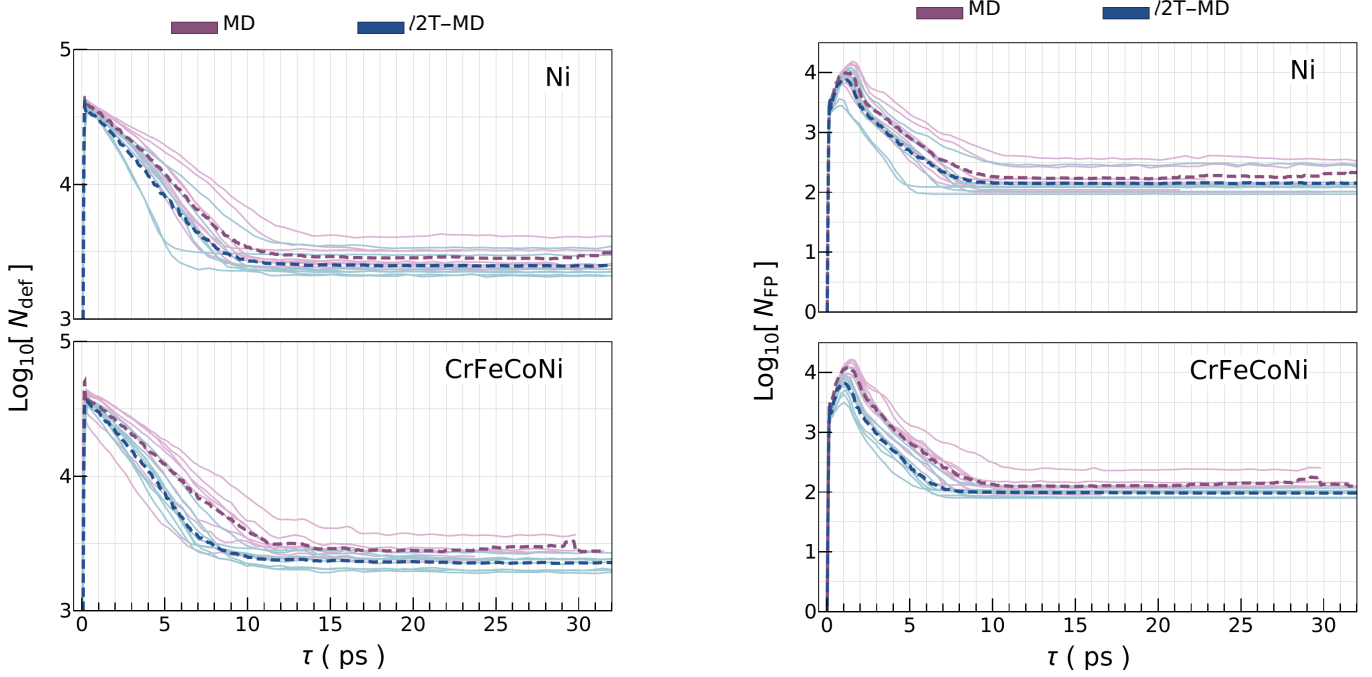


FIG. 10. Time evolution of the total numbers of defected atoms ( $N_{\text{def}}$ ) and Frenkel pairs ( $N_{\text{FP}}$ ) in Ni, and CrFeCoNi within the conventional MD and the  $\ell$ 2T-MD simulations for a 50 keV PKA. Each simulation was repeated eight times to ensure sufficient statistical representation of cascade events.

tropy alloy compared to Ni play a much more modest role in determining the FPs and cluster size. Despite different lattice distortion, the electronic effects reduce  $S_{\text{cluster}}^{\text{max}}$  by  $\sim 125\%$  in CrFeCoNi compared a reduction of  $\sim 80\%$  in Ni.

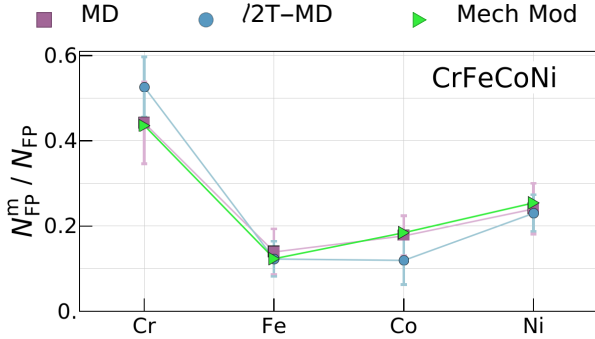


FIG. 12. Fractional FPs of the principal elements in CrFeCoNi after a 50 keV PKA obtained with MD (purple), the  $\ell$ 2T-MD (blue). A simplistic mechanistic model results are also included (green).

Fig. 12 exhibits the steady-state fractions of FPs per principal elements are shown for CrFeCoNi. Even though at the initial stages of the cascade simulation, the FPs are equally distributed in all elements (not shown in the figure), the distribution quickly shifts and reaches the distribution as illustrated in Fig. 12. As clearly portrayed in the graphical representation, Cr disproportionately forms

more FPs while Fe and Co contribute less to the total FPs population. This disparity in the FPs proportion is simply due to lower vacancy and SIA-formation energies of Cr compared to other PEs, as shown in Fig. S12 and Fig. S13. The different FPs fractions open up the question of exploring the compositional space of CrFeCoNi for tuning the electronic and phonon properties to improve the radiation-damage resistance.

To better explain the distribution of FPs in a steady-state, let us use the available information and a simple mechanistic model to predict these fractions. This prediction is insightful because it can help guide non-equimolar HEAs' design for radiation resistance. First, let us define the average vacancy and SIA formation energy denoted as  $\bar{v}^f = \sum_i^{N_e} x_i v_i^f$  and  $\bar{s}_f = \sum_i^{N_e} x_i s_i^f$ , respectively, with  $x_i$  the atomic molar fraction of the HEA. At the same time, let us now assume that the di-vacancy and di-SIA formation energies can be computed. Next, the probably that a FP formation of a given element is given by the following biased probability,  $\rho_i = \exp(-\Delta v_i^f / \bar{v}^f - \Delta s_i^f / \bar{s}_f - \Delta v_i^{2f} / \bar{v}^{2f} - \Delta s_i^{2f} / \bar{s}^{2f})$ . In the biased probability function, the arguments  $\Delta$  are taking with respect to the average value, i.e.,  $\Delta v_i^f = \bar{v}^f - v_i^f$ . The relative changes in formation energies shift the probabilities to generate more FPs of those elements with lower than the average values. Next, the fraction of FPs can be obtained by using the atomic molar fraction of the HEA considered, i.e.,  $x_i^{\text{FP}} = x_i \rho_i$ . Using the values provided above and the described model, we obtained for an equimolar HEA the following concentration of FP defects

	Ni		CrFeCoNi	
	MD	$\ell$ 2T-MD	MD	$\ell$ 2T-MD
$N_{\text{def}}^{\text{max}}$	40042 (683)	37159 (840)	41428 (725)	37216 (827)
$\tau_{\text{def}}^{\text{max}}$	0.31 (0.02)	0.31 (0.01)	0.31 (0.04)	0.30 (0.01)
$N_{\text{def}}^{\text{steady}}$	2828 (174)	2464 (181)	2750 (192)	2246 (97)
$\tau_{\text{def}}^{\text{steady}}$	9.42 (0.80)	9.20 (0.61)	10.17 (0.29)	9.89 (0.24)
$N_{\text{FP}}^{\text{steady}}$	171 (28)	146 (30)	140 (24)	96 (5)
$\tau_{\text{FP}}^{\text{steady}}$	9.20 (0.53)	7.99 (0.63)	9.60 (0.27)	7.50 (0.46)

TABLE I. The mean values and standard error (in brackets) for the maximum number of defected atoms at the peak of the thermal spike ( $N_{\text{def}}^{\text{max}}$ ), at steady state ( $N_{\text{def}}^{\text{steady}}$ ), their corresponding times (in Picoseconds units) ( $\tau_{\text{max}}$ , and  $\tau_{\text{steady}}$ , respectively), the number of Frenkel pairs  $N_{\text{FP}}^{\text{steady}}$  and the dislocation density ( $\rho_{\text{d}}$ ) (in  $m^{-2}$  units) of the formed defects at steady state.

by elements,  $\text{Co}^{\text{FP}} = 0.185$ ,  $\text{Cr}^{\text{FP}} = 0.436$ ,  $\text{Fe}^{\text{FP}} = 0.124$ , and  $\text{Ni}^{\text{FP}} = 0.255$ , which is pretty approximate to the values found by MD while some discrepancy for Co and Cr is seen for  $\ell$ 2T-MD. Thus, while the number of defects can be estimated well with the available models [105], the proposed procedure can be used to estimate the FPs distribution per element.

#### IV. CONCLUSION

This work presented a systematic study of temperature-dependent electronic and phonon properties crucial during defect formation in HEAs in radiation environments. The FCC-phased CrFeCoNi RSS was chosen as the central HEA due to its frequent template material to develop other compositions. It was shown that CrFeCoNi has higher  $G_{\text{e-ph}}$  and  $C_{\text{e}}$  throughout the studied electronic temperate range (up to  $3 \times 10^4$  K) compared to its constituent elements. Using  $\ell$ 2T-MD, we demonstrated that CrFeCoNi was more effective in dissipating excess energy during cascade events via local plasmons, leading to lesser defect formation and higher defect recombination than the elemental Ni. Moreover, this work demonstrated the crucial roles of electronic and phonon effects during cascade events.

Analysis of individual affinity for defect formation of the PEs in CrFeCoNi showed that the elements such as Cr and partially Ni tend to form more FPs due to their relatively lower  $v_{\text{f}}^1$  energies than with the remaining elements. It motivated us to explore the non-equimolar RSS to improve the radiation-damage resistance further. A set of representative non-equimolar RSS compositions were investigated to understand electronic and phonon properties. Lower Cr or Ni concentration (keeping the remaining three PEs equimolar among themselves) lead

to slightly lower  $G_{\text{e-ph}}$  and higher  $\kappa_{\text{e}}$ . Reduction of Fe or Co had negligible effects on  $G_{\text{e-ph}}$ . Moving away from the non-equimolar case led to relatively poorer performance in e-ph-assisted heat dissipation, while it improved energy exchange among electrons of neighboring atoms.

The addition of Al, Mn and Cu to CrFeCoNi was investigated as another strategy. We demonstrated that the equimolar addition of Al substantially increased  $G_{\text{e-ph}}$ , which is a critical factor for plasmon excitations and to reduce defect formation. While the equimolar addition of Mn slightly improved  $G_{\text{e-ph}}$ , the equimolar addition of Cu worsens it. On the other hand, adding any of these elements substantially improved  $\kappa_{\text{e}}$ . These general trends indicated that the addition of lighter elements compared to the averaged atomic mass improves  $G_{\text{e-ph}}$ , considering that atomic mass is used when normalizing phonon modes. On the other hand, the addition of atoms with more differing VEC led to higher  $\kappa_{\text{e}}$  due to higher  $v_{\text{F}}$ , despite shorter-living plasmons when adding lighter elements.

Electronic properties were then integrated into the  $\ell$ 2T-MD model to investigate their effect in FPs formation. We found that the electronic properties play a critical role in determining the steady-state FPs number after the PKA event. Neglecting these effects lead to errors of about 45% between classical MD and  $\ell$ 2T-MD at 50 keV PKA energy. We also investigated the fraction of FPs per principal element in the HEA. We found that elements with smaller vacancy formation energies (i.e., Cr and Ni) resulted in more FPs, whereas elements with higher formation energy (i.e., Fe and Co) showed fewer FPs. This finding suggests the possibility of exploring non-equimolar HEA compositions to obtain optimal radiation resistance combining optimal electronic and lattice properties.

## V. ACKNOWLEDGMENT

We acknowledge the support of New Frontiers in Research Fund (NFRFE-2019-01095) and from the Natural Sciences and Engineering Research Council of Canada (NSERC) through the Discovery Grant under Award Application Number 2016-06114. M.H. gratefully acknowl-

edges the financial support from the Department of Mechanical Engineering at UBC through the Four Years Fellowship. This research partially was supported through computational resources and services provided by Advanced Research Computing at the University of British Columbia.

- 
- [1] B. Cantor, I. Chang, P. Knight, and A. Vincent, *Materials Science and Engineering: A* **375-377**, 213 (2004).
- [2] J.-W. Yeh, S.-K. Chen, S.-J. Lin, J.-Y. Gan, T.-S. Chin, T.-T. Shun, C.-H. Tsau, and S.-Y. Chang, *Advanced Engineering Materials* **6**, 299 (2004).
- [3] J. W. Yeh, *Annales de Chimie. Science des Materiaux* **31**, 633 (2006).
- [4] O. N. Senkov, J. M. Scott, S. V. Senkova, F. Meisenkothen, D. B. Miracle, and C. F. Woodward, *Journal of Materials Science* **47**, 4062 (2012).
- [5] K.-H. Cheng, C.-H. Lai, S.-J. Lin, and J.-W. Yeh, *Thin Solid Films* **519**, 3185 (2011).
- [6] A. Gali and E. George, *Intermetallics* **39**, 74 (2013).
- [7] J. Chen, P. Niu, Y. Liu, Y. Lu, X. Wang, Y. Peng, and J. Liu, *Materials & Design* **94**, 39 (2016).
- [8] X. Xian, Z. Zhong, B. Zhang, K. Song, C. Chen, S. Wang, J. Cheng, and Y. Wu, *Materials & Design* **121**, 229 (2017).
- [9] J. Li, Q. Fang, B. Liu, and Y. Liu, *Acta Materialia* **147**, 35 (2018).
- [10] Y. Cai, G. Wang, Y. Ma, Z. Cao, and X. Meng, *Scripta Materialia* **162**, 281 (2019).
- [11] P.-K. Huang, J.-W. Yeh, T.-T. Shun, and S.-K. Chen, *Advanced Engineering Materials* **6**, 74 (2004).
- [12] C.-Y. Hsu, J.-W. Yeh, S.-K. Chen, and T.-T. Shun, *Metallurgical and Materials Transactions A* **35**, 1465 (2004).
- [13] N. Kumar, M. Fusco, M. Komarasamy, R. Mishra, M. Bourham, and K. Murty, *Journal of Nuclear Materials* **495**, 154 (2017).
- [14] Z. Wu, H. Bei, G. Pharr, and E. George, *Acta Materialia* **81**, 428 (2014).
- [15] B. Gludovatz, A. Hohenwarter, D. Catoor, E. H. Chang, E. P. George, and R. O. Ritchie, *Science* **345**, 1153 (2014).
- [16] Z. Wu, H. Bei, F. Otto, G. Pharr, and E. George, *Intermetallics* **46**, 131 (2014).
- [17] M.-H. Chuang, M.-H. Tsai, W.-R. Wang, S.-J. Lin, and J.-W. Yeh, *Acta Materialia* **59**, 6308 (2011).
- [18] M. W. Ullah, D. S. Aidhy, Y. Zhang, and W. J. Weber, *Acta Materialia* **109**, 17 (2016).
- [19] C.-J. Tong, Y.-L. Chen, J.-W. Yeh, S.-J. Lin, S.-K. Chen, T.-T. Shun, C.-H. Tsau, and S.-Y. Chang, *Metallurgical and Materials Transactions A* **36**, 881 (2005).
- [1] D. F. Rojas, H. Li, O. K. Orhan, C. Shao, J. D. Hogan, and M. Ponga, *Journal of Alloys and Compounds* **893**, 162309 (2022).
- [21] O. K. Orhan, M. Isiet, L. Caparini, and M. Ponga, *Frontiers in Materials* **8** (2022), 10.3389/fmats.2021.816610.
- [22] G. Was and R. Averbach, in *Comprehensive Nuclear Materials*, edited by R. J. Konings (Elsevier, Oxford, 2012) pp. 195–221.
- [23] K.-Y. Tsai, M.-H. Tsai, and J.-W. Yeh, *Acta Materialia* **61**, 4887 (2013).
- [24] X. Zhang, *Cell Biochemistry and Biophysics* **72**, 771 (2015).
- [25] T. Nagase, P. D. Rack, J. H. Noh, and T. Egami, *Intermetallics* **59**, 32 (2015).
- [26] M. Dada, P. Popoola, S. Adeosun, and N. R. Mathe (IntechOpen, 2019).
- [27] S.-q. Xia, Z. Wang, T.-f. Yang, and Y. Zhang, *Journal of Iron and Steel Research International* **22**, 879 (2015).
- [28] O. Deluigi, R. Pasianot, F. Valencia, A. Caro, D. Farkas, and E. Bringa, *Acta Materialia* **213**, 116951 (2021).
- [29] G. Battistoni, T. Boehlen, F. Cerutti, P. W. Chin, L. S. Esposito, A. Fassó, A. Ferrari, A. Lechner, A. Empl, A. Mairani, A. Mereghetti, P. G. Ortega, J. Ranft, S. Roesler, P. R. Sala, V. Vlachoudis, and G. Smirnov, *Annals of Nuclear Energy* **82**, 10 (2015), Joint International Conference on Supercomputing in Nuclear Applications and Monte Carlo 2013, SNA + MC 2013. Pluri- and Trans-disciplinarity, Towards New Modeling and Numerical Simulation Paradigms.
- [30] P. G. Klemens and R. K. Williams, *International Metals Reviews* **31**, 197 (1986).
- [31] J. M. Ziman, *Principles of the Theory of Solids*, 2nd ed. (Cambridge University Press, 1972).
- [32] R. E. B. Makinson, in *Mathematical Proceedings of the Cambridge Philosophical Society*, Vol. 34 (3) (Cambridge University Press, 1938) pp. 474–497.
- [33] N. K. Kumar, C. Li, K. Leonard, H. Bei, and S. Zinkle, *Acta Materialia* **113**, 230 (2016).
- [34] F. Granberg, K. Nordlund, M. W. Ullah, K. Jin, C. Lu, H. Bei, L. M. Wang, F. Djurabekova, W. J. Weber, and Y. Zhang, *Phys. Rev. Lett.* **116**, 135504 (2016).
- [35] C. Lu, L. Niu, N. Chen, K. Jin, T. Yang, P. Xiu, Y. Zhang, F. Gao, H. Bei, S. Shi, M.-R. He, I. M. Robertson, W. J. Weber, and L. Wang, *Nature Communications* **7**, 13564 (2016).
- [36] C. M. Barr, J. E. Nathaniel, K. A. Unocic, J. Liu, Y. Zhang, Y. Wang, and M. L. Taheri, *Scripta Materialia* **156**, 80 (2018).
- [37] Z. Lin and L. V. Zhigilei, *Applied Surface Science* **253**, 6295 (2007), proceedings of the Fifth International Conference on Photo-Excited Processes and Applications.
- [38] D. Duffy and A. Rutherford, *Journal of Physics: Condensed Matter* **19**, 016207 (2006).
- [39] A. Tamm, G. Samolyuk, A. A. Correa, M. Klintonberg, A. Aabloo, and A. Caro, *Phys. Rev. B* **94**, 024305 (2016).
- [40] A. Tamm, M. Caro, A. Caro, G. Samolyuk, M. Klintonberg, and A. A. Correa, *Phys. Rev. Lett.* **120**, 185501 (2018).

- [41] A. Tamm, M. Caro, A. Caro, and A. A. Correa, *Phys. Rev. B* **99**, 174302 (2019).
- [42] E. Zarkadoula, G. Samolyuk, and W. J. Weber, *Materials Research Letters* **7**, 490 (2019).
- [43] E. Zarkadoula, S. L. Daraszewicz, D. M. Duffy, M. A. Seaton, I. T. Todorov, K. Nordlund, M. T. Dove, and K. Trachenko, *Journal of Physics: Condensed Matter* **26**, 085401 (2014).
- [44] E. Zarkadoula, D. M. Duffy, K. Nordlund, M. A. Seaton, I. T. Todorov, W. J. Weber, and K. Trachenko, *Journal of Physics: Condensed Matter* **27**, 135401 (2015).
- [45] E. Zarkadoula, G. Samolyuk, and W. J. Weber, *Journal of Alloys and Compounds* **700**, 106 (2017).
- [46] M. W. Ullah and M. Ponga, *Modelling and Simulation in Materials Science and Engineering* **27**, 075008 (2019).
- [47] M. W. Ullah, N. Sellami, A. Leino, H. Bei, Y. Zhang, and W. J. Weber, *Computational Materials Science* **173**, 109394 (2020).
- [48] J. Grossi, J. Kohanoff, and E. M. Bringa, *Materials Research Express* **7**, 055015 (2020).
- [49] M. Ponga, K. Bhattacharya, and M. Ortiz, *Journal of the Mechanics and Physics of Solids* **95**, 530 (2016).
- [50] M. Ponga, K. Bhattacharya, and M. Ortiz, *Journal of Computational Physics* **407**, 109249 (2020).
- [51] M. Ponga and D. Sun, *Modelling and Simulation in Materials Science and Engineering* **26**, 035014 (2018).
- [52] O. K. Orhan, M. Hendy, and M. Ponga, “Temperature-dependent first-principles electronic, and phonon properties, and molecular dynamics of defect evolution,” <https://github.com/Mponga/Radiation-Damage-in-High-Entropy-Alloys> (2022).
- [53] P. B. Allen, *Phys. Rev. Lett.* **59**, 1460 (1987).
- [54] Z. Li, C. Wang, W. Kang, C. Li, and P. Zhang, *Physics of Plasmas* **22**, 112705 (2015).
- [55] P. Hohenberg and W. Kohn, *Phys. Rev.* **136**, B864 (1964).
- [56] W. Kohn and L. J. Sham, *Phys. Rev.* **140**, A1133 (1965).
- [57] D. C. Langreth and J. P. Perdew, *Phys. Rev. B* **21**, 5469 (1980).
- [58] J. P. Perdew, *Phys. Rev. B* **33**, 8822 (1986).
- [59] J. P. Perdew, J. A. Chevary, S. H. Vosko, K. A. Jackson, M. R. Pederson, D. J. Singh, and C. Fiolhais, *Phys. Rev. B* **46**, 6671 (1992).
- [60] X. Gonze, *Phys. Rev. B* **55**, 10337 (1997).
- [61] X. Gonze and C. Lee, *Phys. Rev. B* **55**, 10355 (1997).
- [62] L. Nordheim, *Annalen der Physik* **401**, 607 (1900).
- [63] V. Heine (Academic Press, 1970) pp. 1–36.
- [64] L. Bellaiche and D. Vanderbilt, *Phys. Rev. B* **61**, 7877 (2000).
- [65] P. Hofmann, I. Y. Sklyadneva, E. D. L. Rienks, and E. V. Chulkov, *New Journal of Physics* **11**, 125005 (2009).
- [66] S. Poncé, E. Margine, C. Verdi, and F. Giustino, *Computer Physics Communications* **209**, 116 (2016).
- [67] M. H. Cohen, *Philosophical Magazine* **3**, 762 (1958).
- [68] O. K. Orhan and D. D. O’Regan, *Journal of Physics: Condensed Matter* **31**, 315901 (2019).
- [69] O. K. Orhan, “Quantum espresso post-processing tool to calculate the drude plasmon energy,” <https://github.com/okorhan/Drude-plasmon-energy> (2020).
- [70] O. K. Orhan and M. Ponga, *The Journal of Physical Chemistry C* **125**, 21521 (2021).
- [71] G. Grimvall, *Physica Scripta* **14**, 63 (1976).
- [72] V. Gasparov and R. Huguenin, *Advances in Physics* **42**, 393 (1993).
- [73] S. Ogawa, H. Nagano, and H. Petek, *Phys. Rev. B* **55**, 10869 (1997).
- [74] S. Dal Forno, L. Ranno, and J. Lischner, *The Journal of Physical Chemistry C* **122**, 8517 (2018).
- [75] I. Y. Sklyadneva, E. V. Chulkov, W.-D. Schöne, V. M. Silkin, R. Keyling, and P. M. Echenique, *Phys. Rev. B* **71**, 174302 (2005).
- [76] P. Giannozzi, S. Baroni, N. Bonini, M. Calandra, R. Car, C. Cavazzoni, D. Ceresoli, G. L. Chiarotti, M. Cococcioni, I. Dabo, A. D. Corso, S. de Gironcoli, S. Fabris, G. Fratesi, R. Gebauer, U. Gerstmann, C. Gougoussis, A. Kokalj, M. Lazzeri, L. Martin-Samos, N. Marzari, F. Mauri, R. Mazzarello, S. Paolini, A. Pasquarello, L. Paulatto, C. Sbraccia, S. Scandolo, G. Sclauzero, A. P. Seitsonen, A. Smogunov, P. Umari, and R. M. Wentzcovitch, *Journal of Physics: Condensed Matter* **21**, 395502 (2009).
- [77] P. Giannozzi, O. Andreussi, T. Brumme, O. Bunau, M. B. Nardelli, M. Calandra, R. Car, C. Cavazzoni, D. Ceresoli, M. Cococcioni, N. Colonna, I. Carnimeo, A. D. Corso, S. de Gironcoli, P. Delugas, R. A. D. Jr, A. Ferretti, A. Floris, G. Fratesi, G. Fugallo, R. Gebauer, U. Gerstmann, F. Giustino, T. Gorni, J. Jia, M. Kawamura, H.-Y. Ko, A. Kokalj, E. Küçükbenli, M. Lazzeri, M. Marsili, N. Marzari, F. Mauri, N. L. Nguyen, H.-V. Nguyen, A. O. de-la Roza, L. Paulatto, S. Poncé, D. Rocca, R. Sabatini, B. Santra, M. Schlipf, A. P. Seitsonen, A. Smogunov, I. Timrov, T. Thonhauser, P. Umari, N. Vast, X. Wu, and S. Baroni, *Journal of Physics: Condensed Matter* **29**, 465901 (2017).
- [78] “Thermo\_pw:Ab-initio computation of material properties,” [https://dalcorso.github.io/thermo\\_pw/](https://dalcorso.github.io/thermo_pw/), accessed: 18.09.2019.
- [79] D. R. Hamann, *Phys. Rev. B* **88**, 085117 (2013).
- [80] M. Schlipf and F. Gygi, *Computer Physics Communications* **196**, 36 (2015).
- [81] D. R. Hamann, M. Schlüter, and C. Chiang, *Phys. Rev. Lett.* **43**, 1494 (1979).
- [82] G. P. Kerker, *Journal of Physics C: Solid State Physics* **13**, L189 (1980).
- [83] D. R. Hamann, *Phys. Rev. B* **40**, 2980 (1989).
- [84] J. Zemann, *Acta Crystallographica* **18**, 139 (1965).
- [85] H. J. Monkhorst and J. D. Pack, *Phys. Rev. B* **13**, 5188 (1976).
- [86] M. Palumbo and A. D. Corso, *Journal of Physics: Condensed Matter* **29**, 395401 (2017).
- [87] We point out that the subindexes  $i$  and  $j$  are used in the  $\ell$ 2T-MD method to denote different atomic sites and should not be confused with traditional notation within the DFT formulations for different orbitals.
- [88] J. P. Mendez and M. Ponga, *Computer Physics Communications* **260**, 107315 (2021).
- [12] S. Plimpton, *Journal of Computational Physics* **117**, 1 (1995).
- [90] D. Farkas and A. Caro, *Journal of Materials Research* **33**, 3218–3225 (2018).
- [91] L. Qian, H. Bao, R. Li, and Q. Peng, *Materials Advances* (2021).
- [92] J. A. Stewart, G. Brookman, P. Price, M. Franco, W. Ji, K. Hattar, and R. Dingreville, *Journal of Applied Physics* **123**, 165902 (2018).

- [93] C.-W. Lee, J. A. Stewart, R. Dingreville, S. M. Foiles, and A. Schleife, *Phys. Rev. B* **102**, 024107 (2020).
- [94] J. F. Ziegler, M. Ziegler, and J. Biersack, *Nuclear Instruments and Methods in Physics Research Section B: Beam Interactions with Materials and Atoms* **268**, 1818 (2010), 19th International Conference on Ion Beam Analysis.
- [95] J. P. Biersack and J. F. Ziegler, in *Ion Implantation Techniques*, edited by H. Ryssel and H. Glawischnig (Springer Berlin Heidelberg, Berlin, Heidelberg, 1982) pp. 122–156.
- [13] M. J. D. Powell, in *Numerical Analysis*, edited by D. F. Griffiths (Springer Berlin Heidelberg, Berlin, Heidelberg, 1984) pp. 122–141.
- [97] H. Tsuzuki, P. S. Branicio, and J. P. Rino, *Computer Physics Communications* **177**, 518 (2007).
- [98] A. Stukowski, *Modelling and Simulation in Materials Science and Engineering* **18**, 015012 (2009).
- [99] A. Stukowski, V. V. Bulatov, and A. Arsenlis, *Modelling and Simulation in Materials Science and Engineering* **20**, 085007 (2012).
- [100] “See Supplemental Materials URL, which includes Refs. [n-m].”.
- [101] M. Born and K. Huang, *Dynamical theory of crystal lattices*, Oxford classic texts in the physical sciences (Clarendon Press, Oxford, 1954).
- [11] F. Mouhat and F. m. c.-X. Coudert, *Phys. Rev. B* **90**, 224104 (2014).
- [103] S. P. Rudin, *Phys. Rev. B* **97**, 134114 (2018).
- [104] Note that the scale for Al is represented at the left of the plot and is several times higher than for the other two elements.
- [105] K. Nordlund, S. J. Zinkle, A. E. Sand, F. Granberg, R. S. Averback, R. Stoller, T. Suzudo, L. Malerba, F. Banhart, W. J. Weber, F. Willaime, S. L. Dudarev, and D. Simeone, *Nature Communications* **9**, 1084 (2018).



# Supplementary Materials

## I. PHASE-STABILITY ASSESSMENT

The mixing Gibbs free energy ( $G_{\text{mix}}$ ) is given for a solid with  $M$  principal elements (PEs) by [S1]

$$G_{\text{mix}} = H_{\text{mix}} + F_{\text{mix}} - TS_{\text{conf}}, \quad (\text{S1})$$

where  $H_{\text{mix}}$ ,  $F_{\text{mix}}$ , and  $S_{\text{conf}}$  are the enthalpy of mixing, the mixing Helmholtz free energy, and the configurational entropy. Using the the enthalpy of mixing of binary bulk metallic glasses ( $H_{ij}$ ),  $H_{\text{mix}}$  is approximately given by [S2],

$$H_{\text{mix}} = \sum_{i < j} 4c_i c_j H_{ij}, \quad (\text{S2})$$

where  $M$ , and  $c_i$  are the number of PEs, and the molar fraction of the  $i$ -th PE.  $H_{ij}$  can be available within the Miedema model in Ref. S3. The second term in Eq. (1) is given by [S4]

$$F_{\text{mix}} = F_M - \sum_i^M c_i F_i, \quad (\text{S3})$$

where  $F_M$ , and  $F_i$  are the Helmholtz free energy of the  $M$ -PEs solid, and its  $i^{\text{th}}$  PE, respectively. For a non-magnetic pristine metal, the Helmholtz free energy is the sum of the electronic, and vibrational contributions,  $F = F_{\text{el}} + F_{\text{vib}}$ . The electronic part is given by [S5–S7]

$$F_{\text{el}} = \int_{-\infty}^{\infty} d\epsilon g(\epsilon) f - \int_{-\infty}^{E_F} d\epsilon \epsilon g(\epsilon) + k_B T \int_{-\infty}^{\infty} d\epsilon g(\epsilon) [f \ln(f) + (1 - f) \ln(1 - f)], \quad (\text{S4})$$

where  $k_B$ , and  $E_F$  are the Boltzmann constant, and the Fermi energy, respectively;  $f = f(\epsilon, T_e)$ , and  $g(\epsilon)$  are the Fermi-Dirac distribution function, and the electronic density of states (DOS) The vibrational part is given by [S8, S9]

$$F_{\text{vib}}(T) = k_B T \int_0^{\infty} d\omega \ln \left[ 2 \sinh \left( \frac{\hbar\omega}{2k_B T} \right) \right] p(\omega), \quad (\text{S5})$$

where  $p(\omega)$  is the phonon DOS. Finally, the configurational entropy is given within the the Stirling approximation by [S10]

$$S_{\text{conf}}^M = -R \sum_i^N c_i \ln(c_i), \quad (\text{S6})$$

where  $R$  is the gas constant.

The necessary and sufficient conditions for the elastic stability of cubic systems are given by [S11]

$$\mathbb{C}_{11} - \mathbb{C}_{12} > 0, \quad \mathbb{C}_{11} + 2 \mathbb{C}_{12} > 0 \text{ and } \mathbb{C}_{44} > 0, \quad (\text{S7})$$

where  $\mathbb{C}_{ij}$  are the elements of the second-order elastic tensor.

## II. ELECTRONIC AND PHONON PROPERTIES

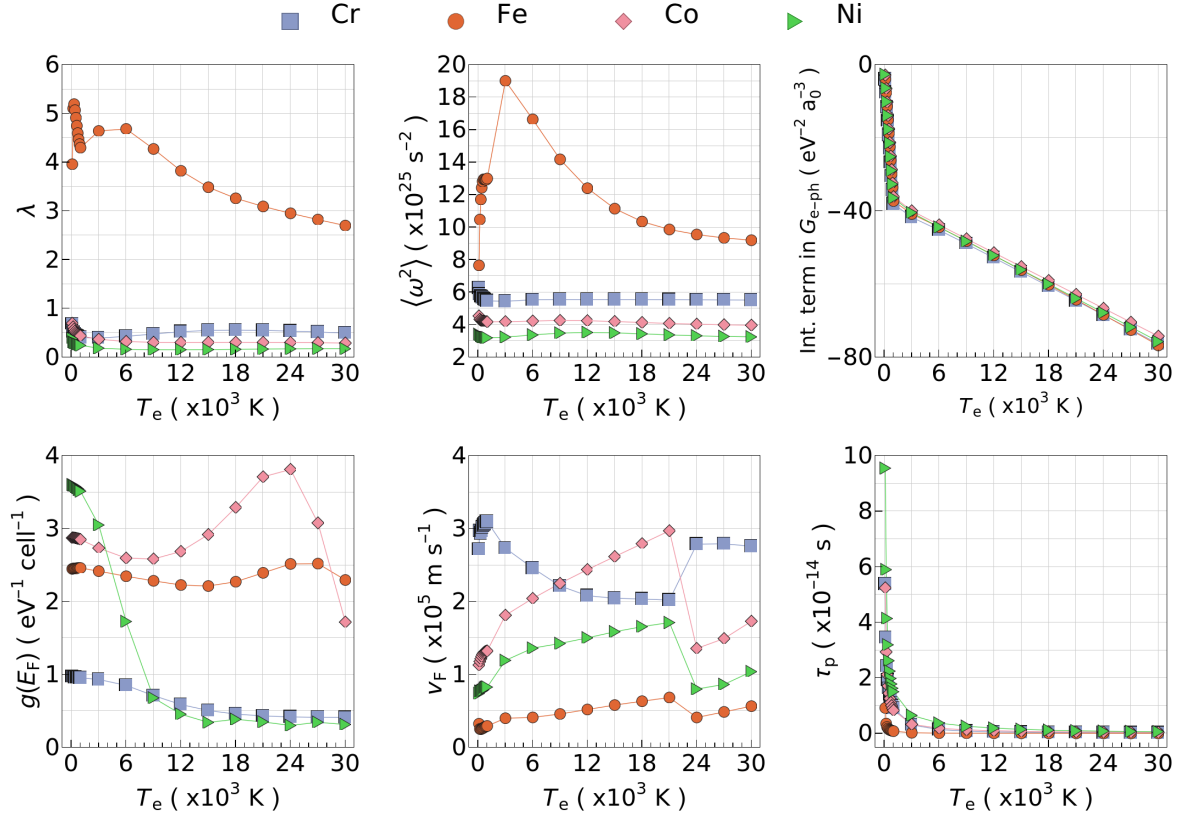


FIG. S1. Temperature dependence of the electronic and phonon quantities, necessary to calculate the electronic specific heat ( $C_e$ ), and the electronic thermal conductivity ( $\kappa_e$ ) of the base principal elements.

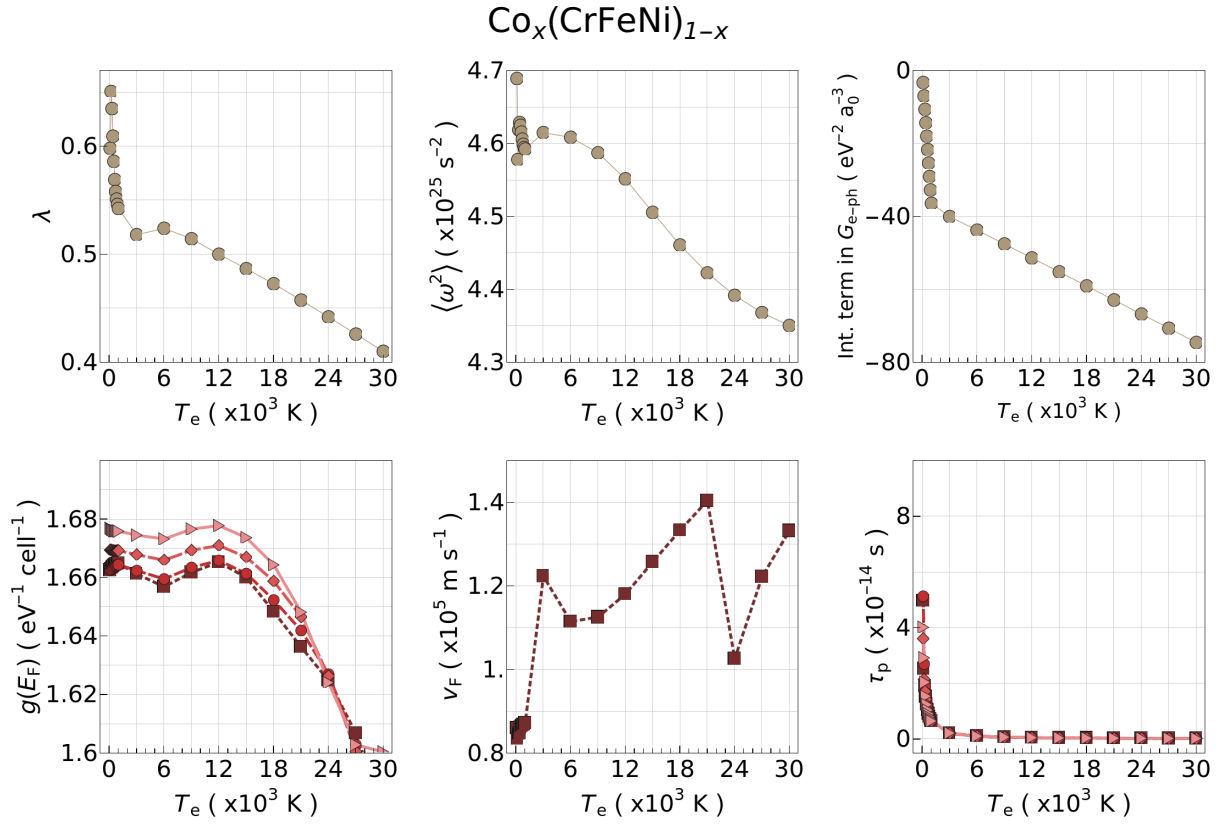


FIG. S2. Temperature dependence of the electronic and phonon quantities, necessary to calculate the electronic specific heat ( $C_e$ ), and the electronic thermal conductivity ( $\kappa_e$ ) of the face-centered cubic CrFeCoNi random solid solution.

### III. COMPOSITION DEPENDENCE OF ELECTRON AND PHONON PROPERTIES

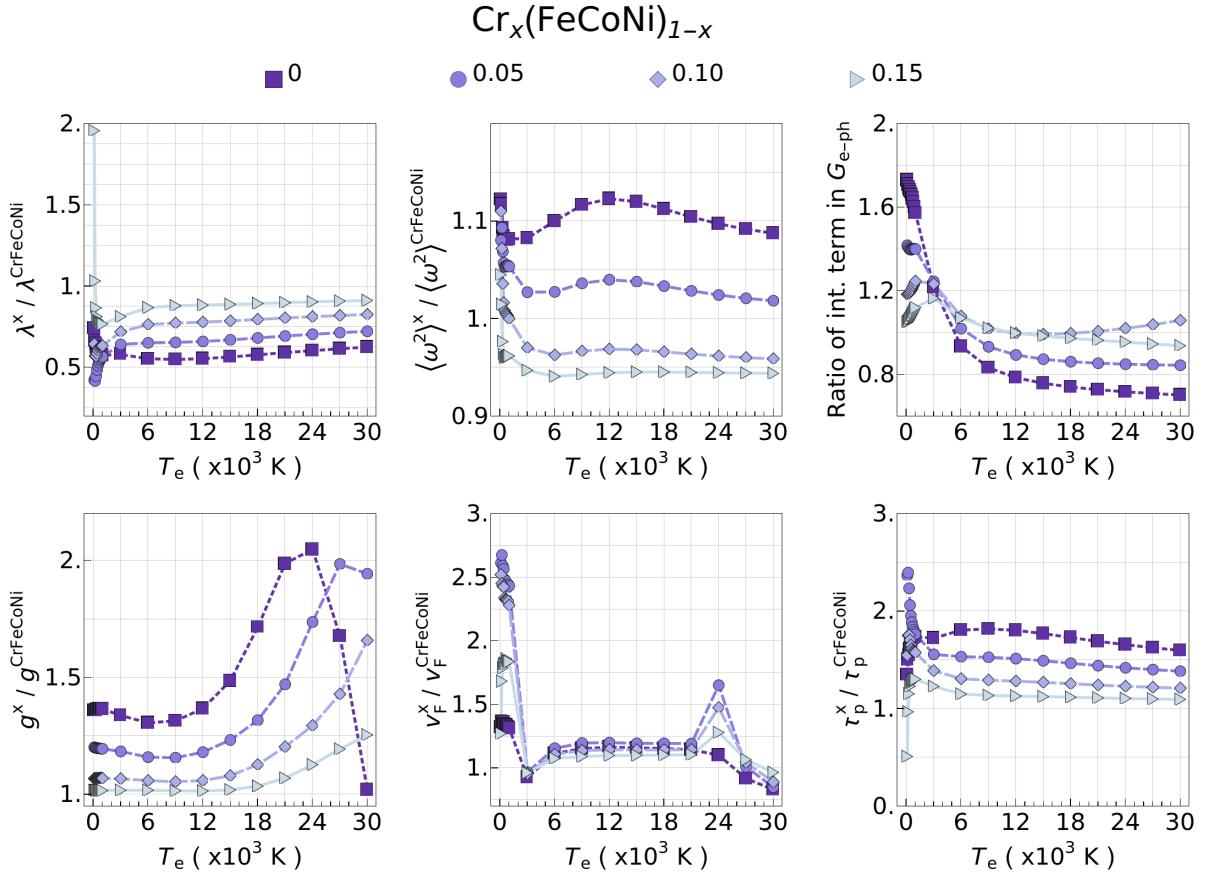


FIG. S3. Temperature dependence of the fractional electronic and phonon quantities, used in calculating the electronic specific heat ( $C_e$ ), and the electronic thermal conductivity ( $\kappa_e$ ), of  $\text{Cr}_x(\text{FeCoNi})_{1-x}$  with respect to those of  $\text{CrFeCoNi}$

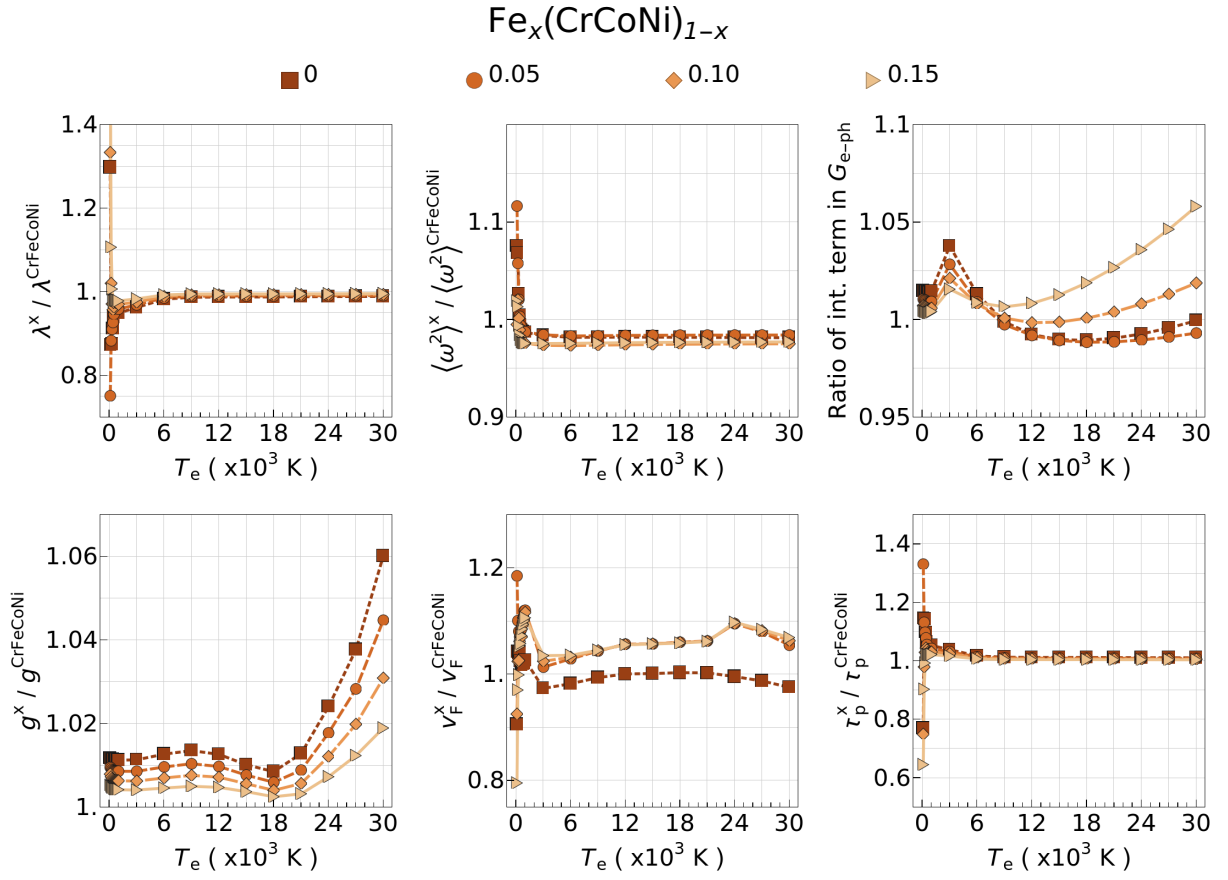


FIG. S4. Temperature dependence of the fractional electronic and phonon quantities, used in calculating the electronic specific heat ( $C_e$ ), and the electronic thermal conductivity ( $\kappa_e$ ), of  $\text{Fe}_x(\text{CrCoNi})_{1-x}$  with respect to those of  $\text{CrFeCoNi}$

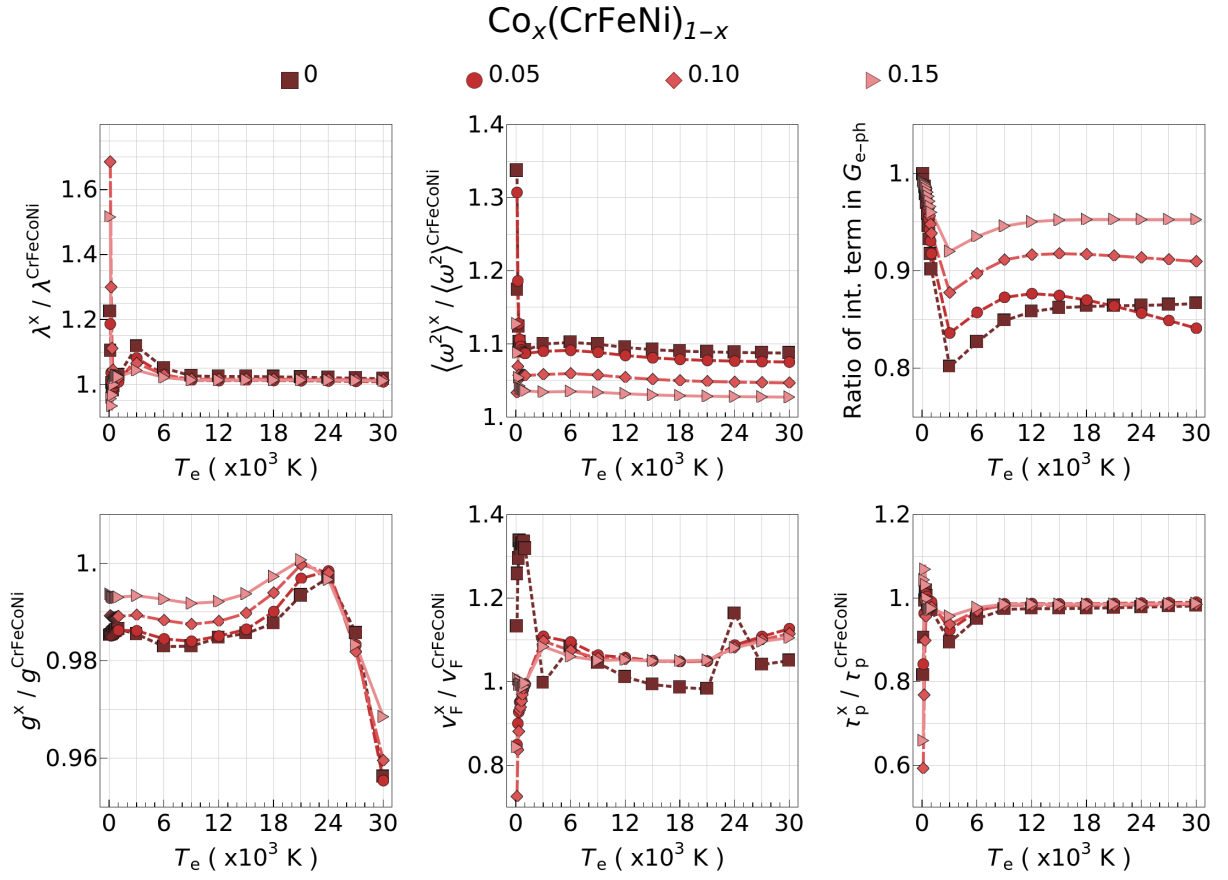


FIG. S5. Temperature dependence of the fractional electronic and phonon quantities, used in calculating the electronic specific heat ( $C_e$ ), and the electronic thermal conductivity ( $\kappa_e$ ), of  $\text{Co}_x(\text{CrFeNi})_{1-x}$  with respect to those of  $\text{CrFeCoNi}$

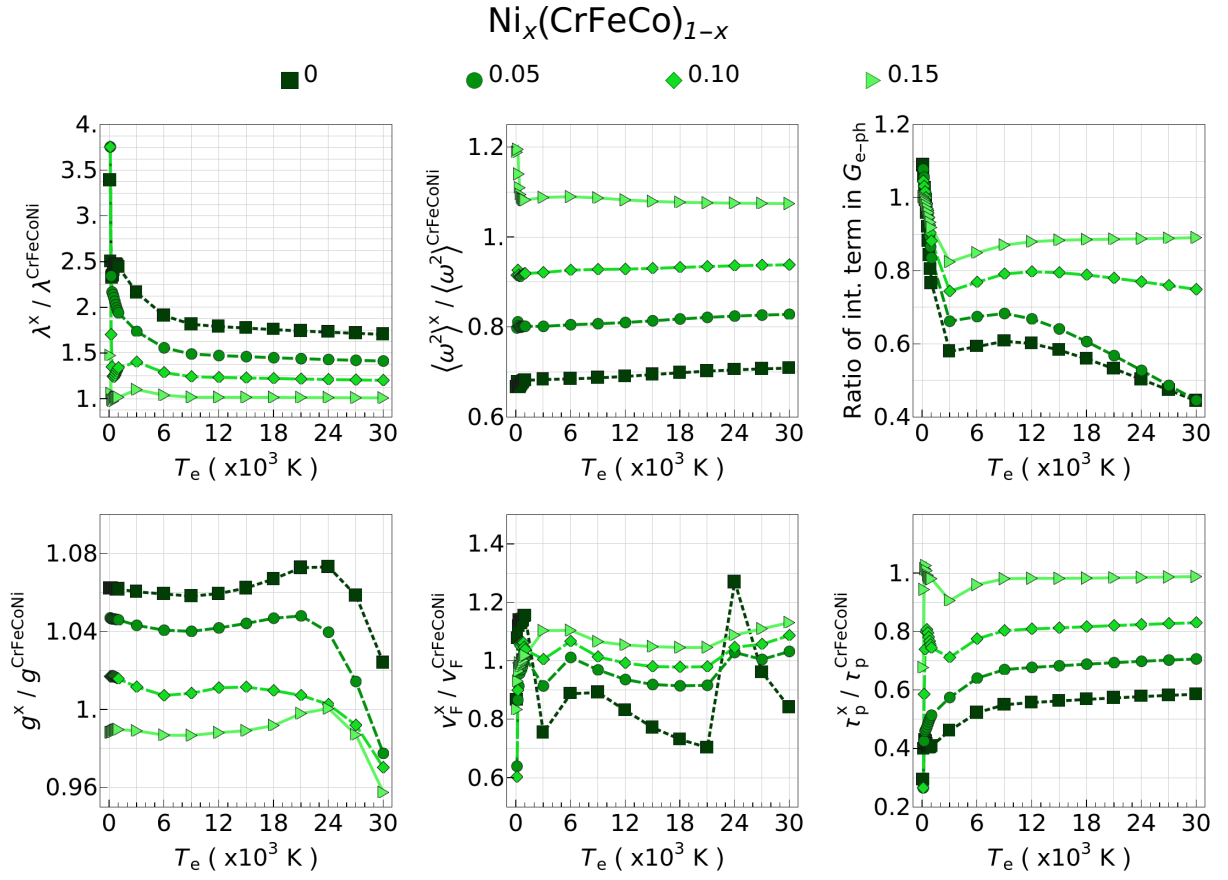


FIG. S6. Temperature dependence of the fractional electronic and phonon quantities, used in calculating the electronic specific heat ( $C_e$ ), and the electronic thermal conductivity ( $\kappa_e$ ), of  $\text{Ni}_x(\text{CrFeCo})_{1-x}$  with respect to those of  $\text{CrFeCoNi}$

## IV. EQUI-MOLAR ADDITION OF AL, MN, OR CU

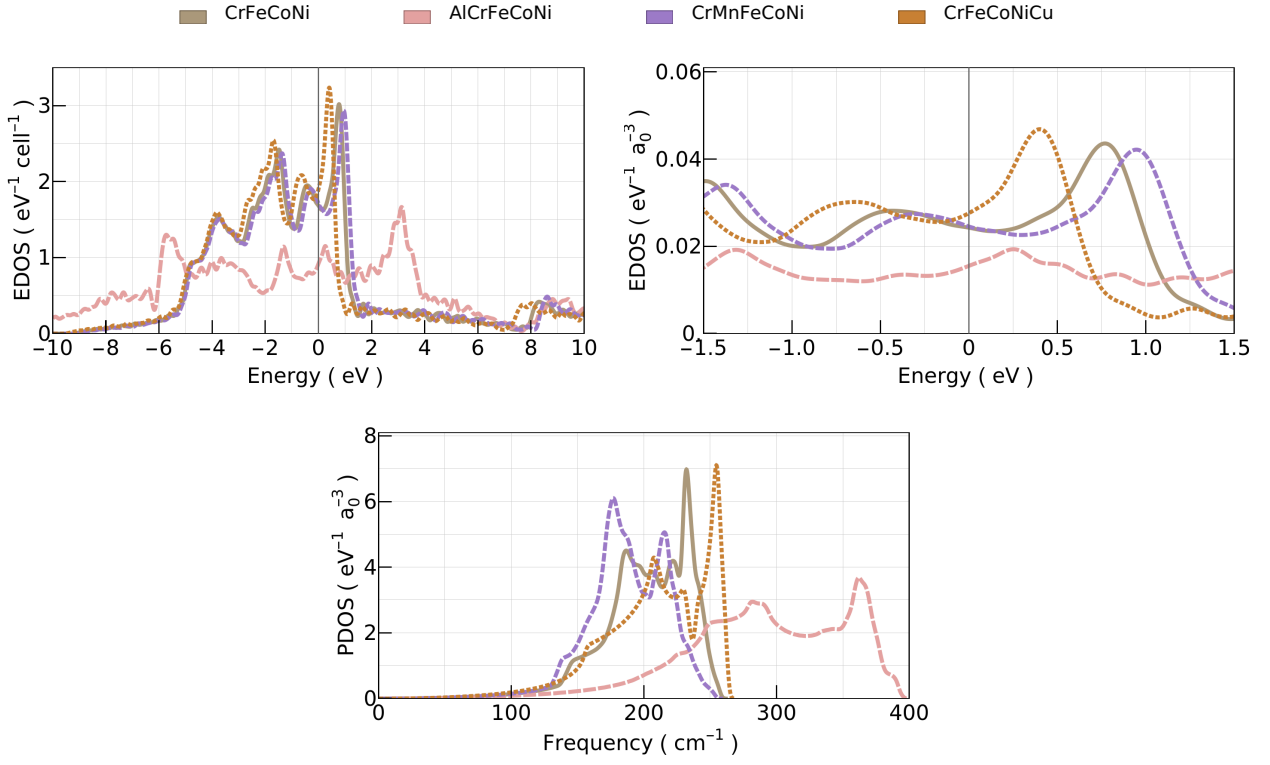


FIG. S7. Electronic density of states (EDOS), and phonon density of states (PDOS) of CrFeCoNi, AlCrFeCoNi, CrMnFeCoNi and CrFeCoNiCu. Fermi level were set to zero in EDOS.



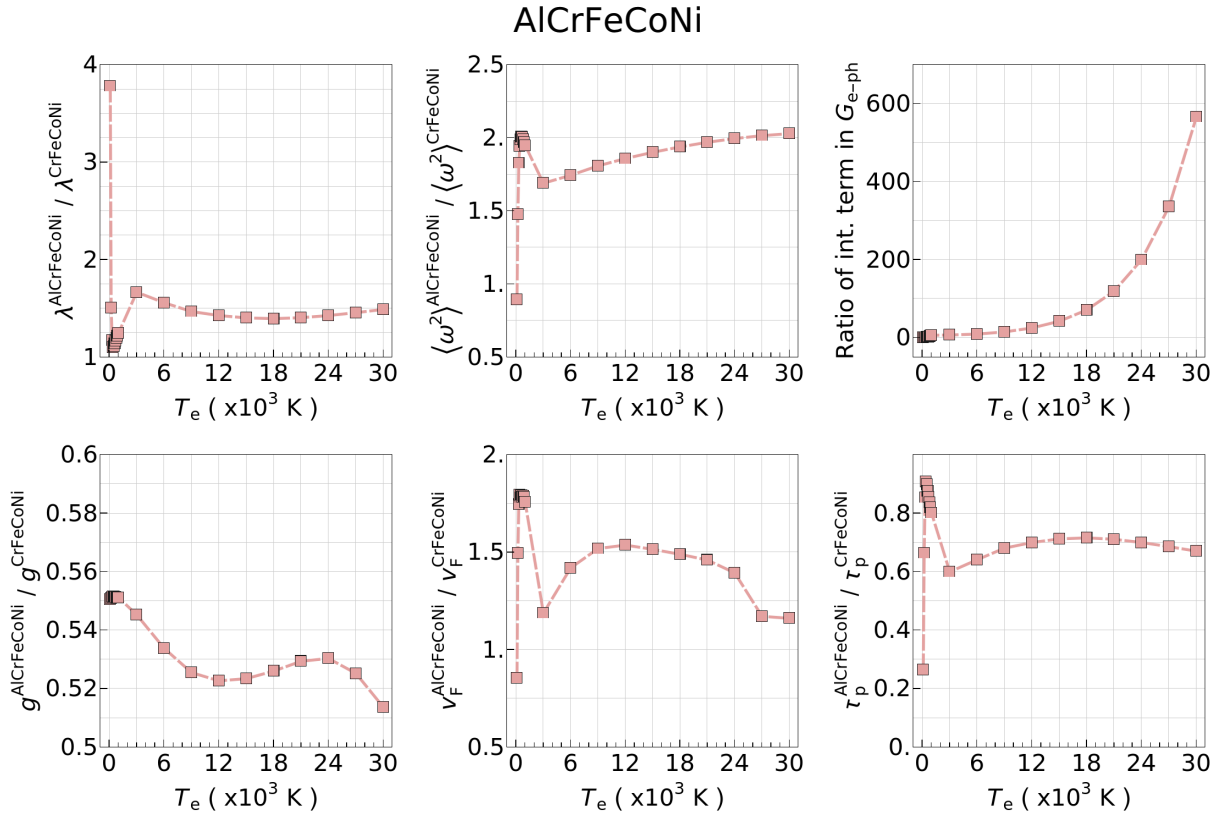


FIG. S8. Temperature dependence of the fractional electronic and phonon quantities, used in calculating the electronic specific heat ( $C_e$ ), and the electronic thermal conductivity ( $\kappa_e$ ), of AlCrFeCoNi with respect to those of CrFeCoNi

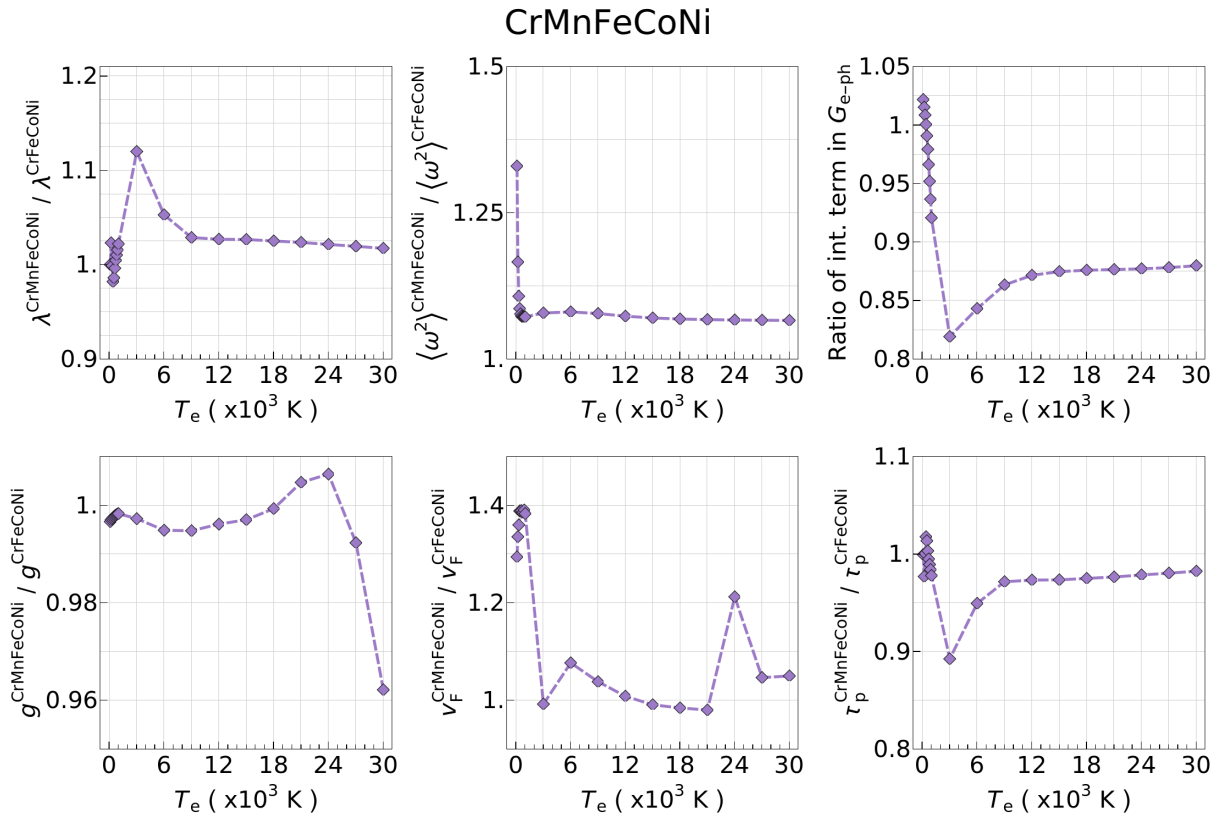


FIG. S9. Temperature dependence of the fractional electronic and phonon quantities, used in calculating the electronic specific heat ( $C_e$ ), and the electronic thermal conductivity ( $\kappa_e$ ), of CrMnFeCoNi with respect to those of CrFeCoNi

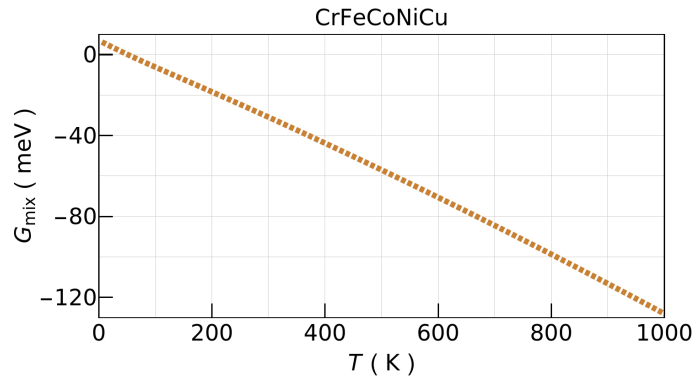


FIG. S10. Temperature dependence of the mixing Gibbs free energy ( $G_{\text{mix}}$ ) of the random solid solutions of CrFeCoNiCu.

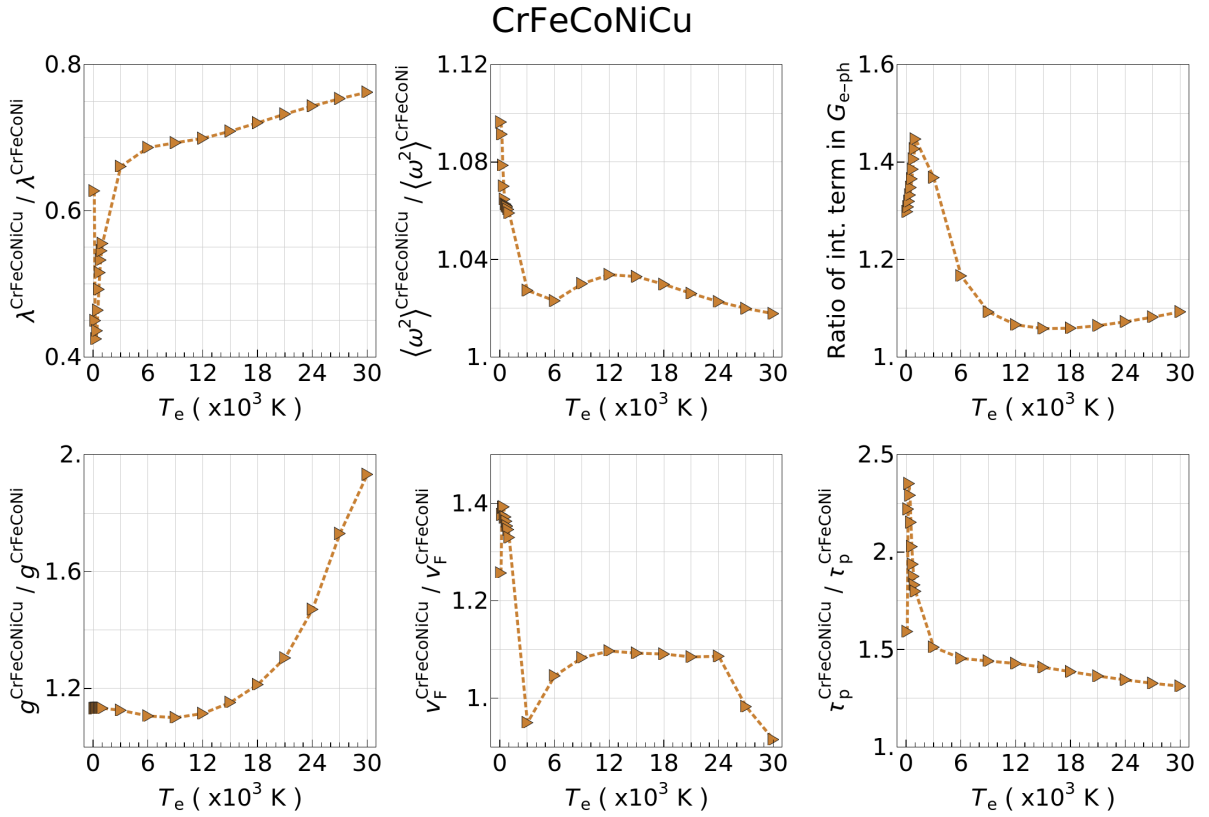


FIG. S11. Temperature dependence of the fractional electronic and phonon quantities, used in calculating the electronic specific heat ( $C_e$ ), and the electronic thermal conductivity ( $\kappa_e$ ), of CrFeCoNiCu with respect to those of CrFeCoNi

## V. TIME EVOLUTION OF DEFECT FORMATION IN NI, AND CRFECONI

	Ni		CrFeCoNi	
	MD	$\ell$ 2T-MD	MD	$\ell$ 2T-MD
$\tau$ at $T_{\text{lat}}^{\text{dip}}$	0.25	0.24	0.25	0.24
$T_{\text{lat}}^{\text{dip}}$	344	340	346	340
$T_{\text{el}}$ at $T_{\text{lat}}^{\text{dip}}$	-	304	-	306
$T_{\text{lat}}^{\text{steady}}$	355	334	356	332
$T_{\text{el}}^{\text{steady}}$	-	329	-	331

TABLE S1. Critical points of the averaged  $T_{\text{avr}}$ , and  $T_{\text{loc}}^{\text{max}}$  curves.

## VI. SELF-INTERSTITIAL ATOM AND VACANCY FORMATION ENERGIES OF THE BASE ELEMENTS

Mono- and di-vacancy and self-interstitial atom (SIA) formation energy of each element in a CrFeCoNi simulation cells were calculated using molecular statics method in the Large-scale Atomic/Molecular Massively Parallel Simulator (LAMMPS) software [S12]. The simulation cells were subjected to energy minimization at  $T = 0$  K using the Polak-Ribière conjugate gradient algorithm [S13]. The calculations were repeated randomly for up to 1000 different atomic sites to explore the statistical distribution of the formation energy of each element. The SIA sites studied are the  $\langle 100 \rangle$  dumbbell interstitial sites which was shown previously to be the most stable Self-interstitial with the lowest

formation energy [S14]. Point defect energies, including vacancy and SIA di-vacancy and di-SIA formation energies were calculated using the following equations

$$v_f^i = E_f(N - i) - \left[ \frac{N_0 - i}{N_0} \right] E_0, \quad (\text{S8})$$

$$s_f^i = E_f(N + i) - \left[ \frac{N_0 + i}{N_0} \right] E_0, \quad (\text{S9})$$

where  $v_f^i$  and  $s_f^i$  are the point defect formation energies,  $E_0$  is the cohesive energy per atom in the bulk, and  $E_f(N - i)$  is the total energy in the simulation cell when the point defects are introduced.  $N_0 = 702,464$  is the initial number of atoms in the simulation cells,  $i$  is the number of added or removed atoms, which is  $i = 1$  for mono-vacancy formation energy  $v_f^1$  and mono-SIA formation energy  $s_f^1$  and  $i = 2$  for di-vacancy formation energy  $v_f^2$  and di-SIA formation energy  $s_f^2$ .

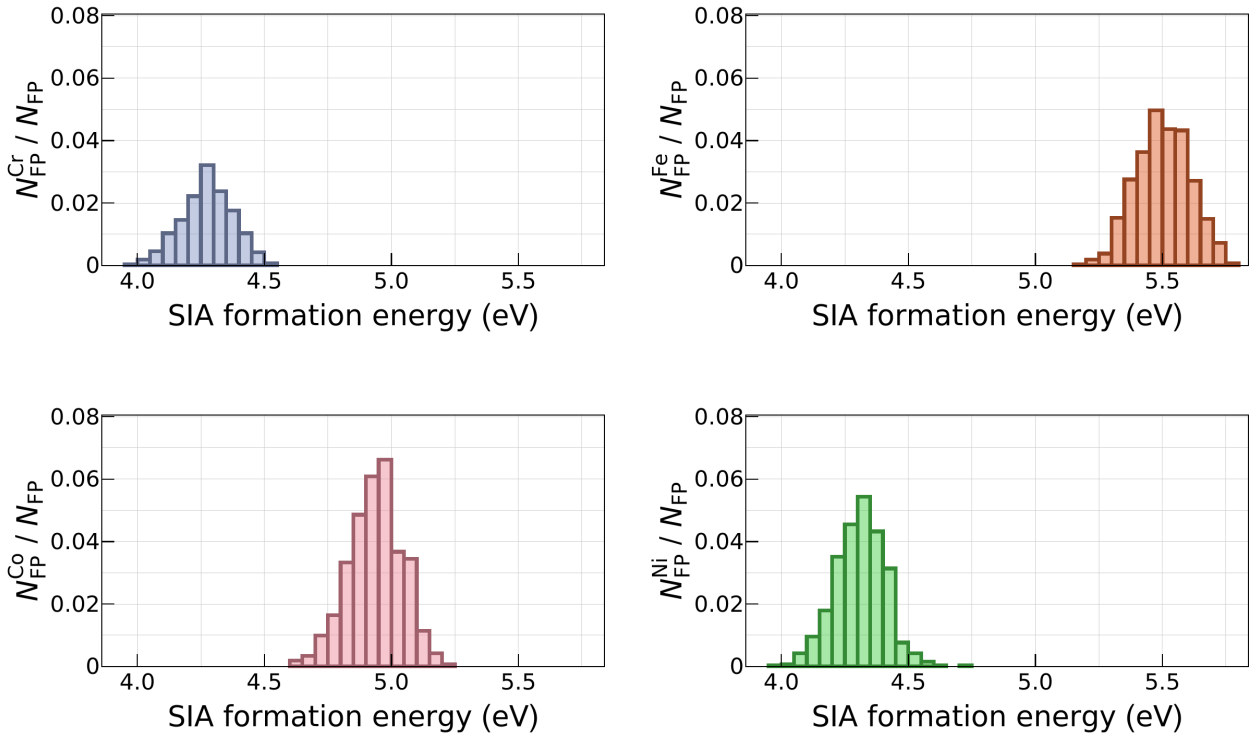


FIG. S12. Mono-self-interstitial atom (SIA) formation energies( $s_f^1$ ) of the principal element of CrFeCoNi, calculated in CrFeCoNi environment.

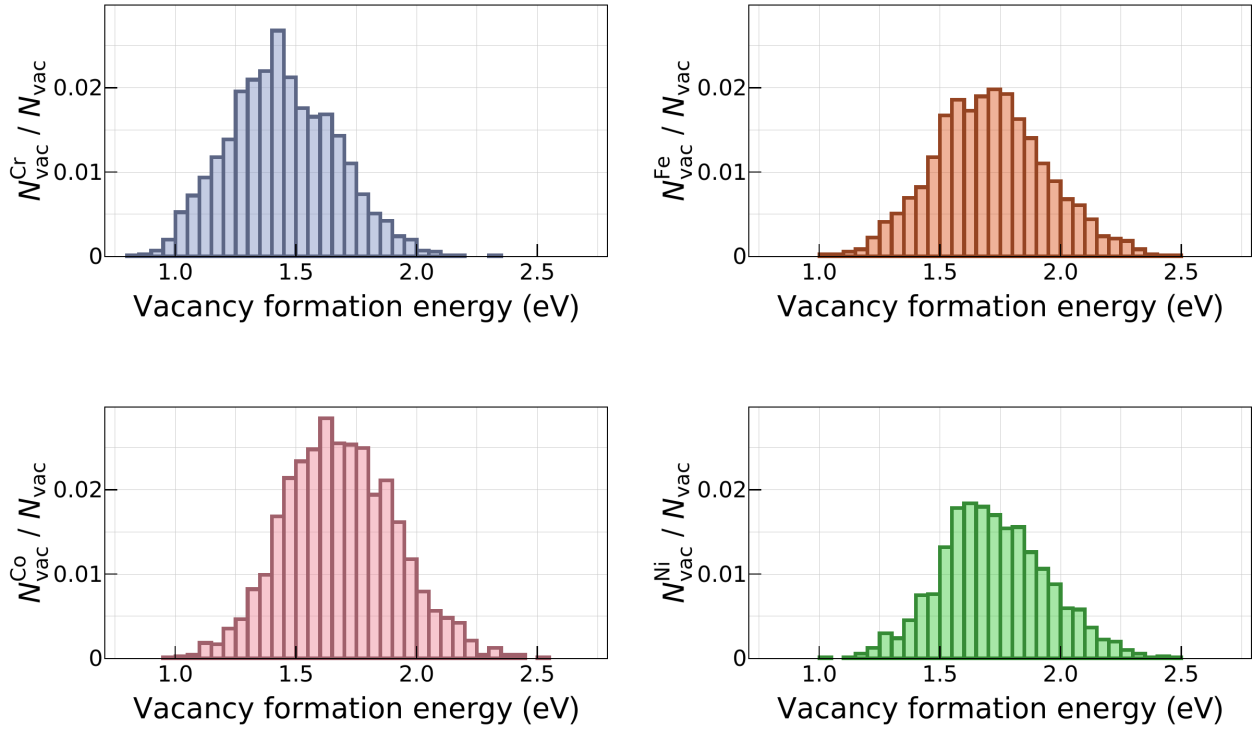


FIG. S13. Mono-vacancy formation energies ( $v_f^1$ ) of the principal element of CrFeCoNi, calculated in CrFeCoNi environment.

	$v_f^1$	$v_f^2$	$s_f^1$	$s_f^2$
Cr	1.46 (0.23)	2.99 (0.30)	4.27 (0.10)	13.38 (0.62)
Fe	1.71 (0.23)	3.38 (0.33)	5.51 (0.11)	15.65 (1.25)
Co	1.69 (0.23)	3.24 (0.32)	4.94 (0.10)	14.95 (0.78)
Ni	1.70 (0.22)	3.31 (0.31)	4.31 (0.10)	13.19 (0.67)

TABLE S2. The mean values and standard deviation (in brackets) for  $v_f^1$ ,  $v_f^2$ ,  $s_f^1$  and  $s_f^2$ .

## VII. DEFECT CLUSTERING

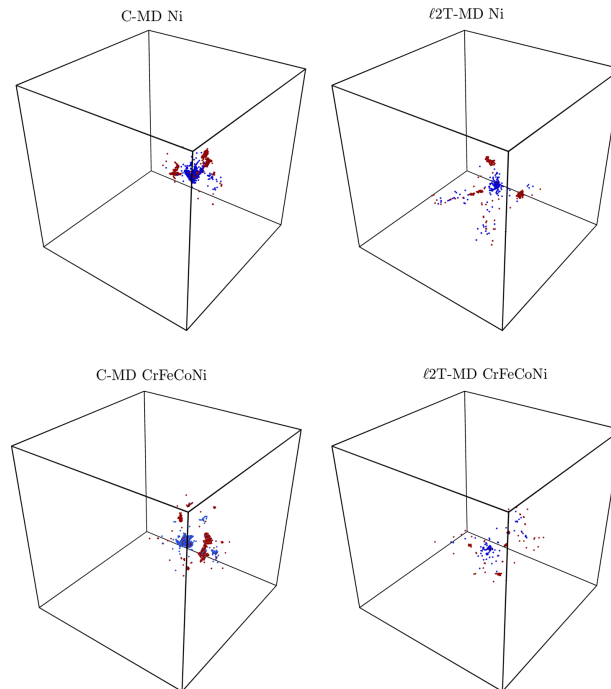


FIG. S14. Self-interstitial atom (in red), and vacancy (in blue) populations at the steady states of Ni, and CrFeCoNi within the conventional MD and the  $\ell 2T$ -MD simulations.

- 
- [S1] D. F. Rojas, H. Li, O. K. Orhan, C. Shao, J. D. Hogan, and M. Ponga, *Journal of Alloys and Compounds* **893**, 162309 (2022).
- [S2] K. M. Youssef, A. J. Zaddach, C. Niu, D. L. Irving, and C. C. Koch, *Materials Research Letters* **3**, 95 (2015).
- [S3] A. Takeuchi and A. Inoue, *MATERIALS TRANSACTIONS* **46**, 2817 (2005).
- [S4] A. Fernández-Caballero, M. Fedorov, J. S. Wróbel, P. M. Mummery, and D. Nguyen-Manh, *Entropy* **21** (2019), 10.3390/e21010068.
- [S5] Y. Wang, Z.-K. Liu, and L.-Q. Chen, *Acta Materialia* **52**, 2665 (2004).
- [S6] L. Landau and E. Lifshitz, “Statistical physics,” (Pergamon Press, Headington Hill Hall, Oxford, OX3 0BW England, 1980) Chap. 5, pp. 158–168, 3rd ed.
- [S7] F. Tian, *Frontiers in Materials* **4**, 36 (2017).
- [S8] A. van de Walle and G. Ceder, *Rev. Mod. Phys.* **74**, 11 (2002).
- [S9] S.-L. Shang, Y. Wang, D. Kim, and Z.-K. Liu, *Computational Materials Science* **47**, 1040 (2010).
- [S10] L. J. Santodonato, Y. Zhang, M. Feygenson, C. M. Parish, M. C. Gao, R. J. K. Weber, J. C. Neufeind, Z. Tang, and P. K. Liaw, *Nature Communications* **6**, 5964 EP (2015), article.
- [S11] F. Mouhat and F. m. c.-X. Coudert, *Phys. Rev. B* **90**, 224104 (2014).
- [S12] S. Plimpton, *Journal of Computational Physics* **117**, 1 (1995).
- [S13] M. J. D. Powell, in *Numerical Analysis*, edited by D. F. Griffiths (Springer Berlin Heidelberg, Berlin, Heidelberg, 1984) pp. 122–141.
- [S14] O. Deluigi, R. Pasianot, F. Valencia, A. Caro, D. Farkas, and E. Bringa, *Acta Materialia* **213**, 116951 (2021).